

Graphical Abstract

Geometric Reinitialization for Capillary Flows: a Comparative Study with State-of-the-Art Conservative Level-Set Methods

Hélène Papillon-Laroche, Amishga Alphonius, Magdalena Schreter-Fleischhacker,
Jean-Philippe Harvey, Bruno Blais

Highlights

Geometric Reinitialization for Capillary Flows: a Comparative Study with State-of-the-Art Conservative Level-Set Methods

Hélène Papillon-Laroche, Amishga Alphonius, Magdalena Schreter-Fleischhacker,
Jean-Philippe Harvey, Bruno Blais

- Comparison of PDE-based, projection-based and geometric reinitialization
- Geometric method provides a two-parameters framework leading to high-quality results
- PDE-based approach achieves high-quality results, but the four hyper-parameters selection is case-dependent
- Projection-based method fails for 3D capillary flows
- Sensitive metrics of interest based on the shape of the interface are required for a meaningful comparison

Geometric Reinitialization for Capillary Flows: a Comparative Study with State-of-the-Art Conservative Level-Set Methods

Hélène Papillon-Laroche^a, Amishga Alphonius^a, Magdalena Schreter-Fleischhacker^b, Jean-Philippe Harvey^c, Bruno Blais^a

^a*CHAOS Laboratory, 2500 Chemin de Polytechnique, Montréal, H3T 1J4, Québec, Canada*

^b*Professorship of Simulation for Additive Manufacturing, Technical University of Munich, Freisinger Landstraße 52, Garching, 85748, Germany*

^c*Centre de recherche en calcul thermochimique (CRCT), Polytechnique Montréal, 2500 Chemin de Polytechnique, Montréal, H3T 1J4, Québec, Canada*

Abstract

Simulations of immiscible flows involving surface tension (ST) require a robust high-fidelity framework. State-of-the-art multi-phase models, such as the Conservative Level-Set (CLS) approach, rely on Eulerian representations of the fluids and interface and require reinitialization methods to ensure volume conservation and accurate ST force modeling. This work focuses on the complete description of a CLS solver and proposes a novel geometric reinitialization method, based on the level-set literature. It includes a quantitative and objective comparison of this new geometric method to two reinitialization approaches: the PDE-based reinitialization proposed in the original CLS method and a simple projection-based approach. This comparison tackles three 3D application cases: the rise of a bubble, the capillary migration of a droplet, and the Rayleigh-Plateau instability development in a capillary jet. The PDE-based and geometric methods lead to high-quality,

spatially-converged results in good agreement with benchmark and analytic solutions, while the projection-based reinitialization fails to capture complex 3D interfacial dynamics. The results also highlight the robustness of the novel geometric method which offers a two-parameter framework in comparison to the PDE-based method that necessitates a case-dependent selection of four parameters.

Keywords:

Computational Fluid Dynamics (CFD), Multi-phase flows, Capillary driven flows, Conservative Level-Set (CLS), Reinitialization

1. Introduction

At length scales approaching and below the capillary length, surface tension (ST) drives immiscible flows [1]. This commonly occurs in many multiphase applications including droplets and bubbles [2] or metal additive manufacturing processes [3]. The current work focuses on incompressible interfacial flows.

The incompressible Navier-Stokes (NS) equations govern the dynamics of each fluid phase. The ST force results in a jump in the stress tensor at the interface between the two fluids. The magnitude of this jump depends on the interfacial properties of the material (i.e., the ST coefficient and its derivatives with respect to temperature and/or composition) as well as the curvature of the interface.

In most capillary-driven flows, the interface moves and deforms, making a boundary (interface) conforming approach challenging, in particular due to re-meshing requirements when the interface presents large deformations,

breaks-up or coalesces [2]. Considering this, one-fluid approaches relying on a Eulerian description of the phases are usually preferred to two-fluid models.

Single fluid models treat the jump boundary condition as a singular force on the right-hand side of the NS momentum equation. However, the position and geometric properties of the moving interface are unknowns. Hence, simulations require an additional interface solver coupled to the typical NS solver. Current available methods range from Lagrangian to Eulerian descriptions of the interface [2].

The Eulerian interface representation uses a phase indicator ϕ to capture the transport of the interface with the flow. It corresponds to a diffuse-interface framework, which regularizes the sharp interface, discontinuous property fields, and the ST force over a given thickness [4] using a smoothing function.

The Eulerian description of the interface with the phase indicator varies among the scientific literature. The Level-Set (LS) method employs a signed-distance function with the interface corresponding to $\phi = 0$ [5]. The Volume-Of-Fluid (VOF) method uses the phase fraction, typically ranging from 0 to 1, changing rapidly and smoothly from one extremum to the other at the interface, represented by the iso-contour $\phi = 0.5$. The Conservative Level-Set (CLS) approach [6] considers a similar description as the VOF, however, the phase indicator represents a pseudo-signed-distance instead of a fluid fraction.

The advection of the phase indicator with the velocity field models the transport of the interface [7, 8]. Coupling with the NS momentum equation also happens through the change in physical properties (density and viscos-

ity) at the interface and the ST force [7]. Regularized formulations of these discontinuous fields rely on smooth approximations of the Heaviside function $H_\Gamma(\phi)$ and Dirac Delta distribution $\delta_\Gamma(\phi)$ [2].

This regularization introduces modeling error in the resolution of the NS equations. Fuster and Mimoh [4] work provides an error estimator for the resolution of elliptic problems with regularized discontinuous diffusion coefficients. They show first order convergence of the error on the solution with respect to the interface thickness. While theoretical results are not available for complex problems such as two-phase flows, the findings support that limiting the interface thickness to a resolvable value, i.e., the cell size h , could decrease the modeling errors. This model error occurs regardless of which of method (e.g., LS, VOF, or CLS) is used. Hence, such framework should ideally keep a constant interface thickness $\Delta_\Gamma = \mathcal{O}(h)$ throughout the simulation.

However, the space and time discretizations of typical numerical schemes as well as stabilization methods (or limiters) add artificial diffusion in the problem. Without any self-sharpening term or specific advection schemes, it results in the thickening and smearing of the interface as the simulation time progresses [9, 5].

Another challenge lies in volume conservation. In the LS method, the advection of the phase indicator leads to the loss of its signed distance function properties. It distorts (e.g., stretches or compresses) the phase indicator field and results in a non-conservative behavior [5].

Simple advection schemes using the phase indicator description of the

VOF or CLS methods conserve the global volume defined as:

$$V_{\text{global}} = \int_{\Omega} \phi d\Omega$$

However, when considering the volume of the domain enclosed by the $\phi = 0.5$ iso-contour, denoted Ω_1 ,

$$V = \int_{\Omega_1} 1 d\Omega$$

non-conservative behavior can be observed. This leads to artificial volume transfer between the two phases [10].

Therefore, Eulerian frameworks need mechanisms to mitigate the smearing of the interface and volume losses and gains. Available strategies include:

- **Specialized advection schemes.** Conservation of the phase fluxes across cell boundaries reduces excessive diffusion in the original VOF method by Hirt and Nichols [9] and later developments. It relies on interface reconstruction and specific advection schemes [5]. Standard schemes found in the Continuous Galerkin (CG) Finite Element Method (FEM) are unsuitable for such specialized framework [6].
- **Improved discretizations.** Simulations of single-phase flows can benefit from high-order methods. However, in the case of fluid-fluid flows with ST, the discontinuities at the interface reduce the convergence rate of the solution [5, 11, 12]. A smaller cell size increases the accuracy of the interface position and helps reduce numerical diffusion [6], but uniform refinement has a significant computational cost. Dynamic mesh adaptation offers a suitable alternative which increases the cell density in high error areas, while applying coarsening to the

cells in low error regions. This process requires adequate error estimation to identify where the interface should be refined.

- **Reinitialization methods.** For LS and CLS methods, most authors turn to reinitialization procedures to preserve the interface quality and volume conservation while keeping a simple advection scheme [6, 10, 13, 14]. In a LS framework, they aim at regaining a signed distance function either by a direct geometric computation of the latter [13, 14] or by the resolution of a PDE enforcing $\|\nabla\phi\| = 1$ [5]. For the CLS method, the original work of Olsson et al. [6] uses a PDE-based reinitialization which balances compressive and diffusive terms in the normal direction of the interface.

In the context of a FEM framework, dynamic mesh adaptation and reinitialization procedures are suitable methods to mitigate the excessive interface diffusion and non-conservative behavior. For the reinitialization procedure, there are multiple available methods, e.g., [7]:

- PDE-based methods proposed in a CLS context, for example, the aforementioned original CLS method by Olsson et al. [6] and improved versions, such as the Accurate CLS (ACLS) by Desjardins et al. [15] and a reformulation of the CLS method by Chiodi and Desjardins [16];
- projection-based methods for CLS frameworks which project ϕ in a sharper space such as proposed by Aliabadi and Tezduyar [10];
- PDE-based methods proposed in an LS context, such as originally proposed by Sussman et al. [17];

- geometric redistanciation for LS methods, for example, the ones proposed by Ausas et al. [13] and Henri et al. [14].

For both LS and CLS approaches, simple reinitialization methods (e.g. Olsson et al. [6]), come at the cost of artificial displacement of the interface [5]. However, some of the aforementioned approaches tackling this challenge, e.g., the reformulated CLS method by Chiodi and Desjardins [16], lead to a complex implementation and a higher computational cost [7]. A gap in the current literature lies in the absence of comparative studies between reinitialization methods for realistic application cases: it is challenging to objectively assess the suitability of available methods since they are generally implemented in completely different numerical frameworks.

This work presents a simple and robust two-phase flow solver in a FEM framework that is capable of both 2D and 3D simulations. It includes dynamic mesh adaptation as well as three different reinitialization procedures: a PDE-based reinitialization following the work of Olsson et al. [6], a new geometric reinitialization method based on the LS literature [13], and a projection-based approach proposed by Aliabadi and Tezduyar [10]. It also provides an objective and quantitative comparison of these three reinitialization methods to assess their suitability and robustness.

The paper takes the following structure: first, Section 2 presents the problem formulation, along with the treatment of interfacial physical property changes, the ST force model, and the description the general solver. The presentation of the three reinitialization procedures follows in Section 3. Finally, Section 4 presents the results and quantitative comparisons of the reinitialization methods for three three-dimensional application cases: the

rising bubble benchmark [18, 19], the capillary migration of a droplet [20], and the Rayleigh-Plateau instability [21].

2. Problem formulation

The problem formulation described in this work considers a one-fluid framework with an Eulerian interface representation. The domain of interest is $\Omega = \Omega_0 \cup \Omega_1$, where each subscript $i \in \{0, 1\}$ is one fluid. The fluid-fluid interface is denoted by Γ and the domain boundary by $\partial\Omega$.

For simplicity, the following finite element formulations use the inner product notations in the weak forms [22]:

$$\begin{aligned} (a, b)_\Omega &= \int_\Omega a \cdot b \, d\Omega \\ (\nabla \mathbf{a}, \nabla \mathbf{b})_\Omega &= \int \nabla \mathbf{a} : \nabla \mathbf{b} \, d\Omega \\ (a, b)_{\Omega_k} &= \sum_k \int_{\Omega_k} a \cdot b \, d\Omega_k \end{aligned}$$

where $\sum_k \int_{\Omega_k} \cdot \, d\Omega_k$ represents the sum of the integral over all k elements (Ω_k) of the mesh.

2.1. Navier-Stokes Equations

The *strong formulation* of the incompressible NS equations considered in this work is:

$$\nabla \cdot \mathbf{u} = 0 \quad \forall \mathbf{x} \in \Omega \times (0, t_{\text{end}}] \quad (1)$$

$$\rho \left(\frac{\partial \mathbf{u}}{\partial t} + (\mathbf{u} \cdot \nabla) \mathbf{u} \right) = \nabla \cdot \boldsymbol{\sigma} + \mathbf{F}_\Gamma + \rho \mathbf{g} \quad \forall \mathbf{x} \in \Omega \times (0, t_{\text{end}}] \quad (2)$$

where \mathbf{u} is the velocity vector and $\boldsymbol{\sigma} = -p \mathbf{I} + \mu \left(\nabla \mathbf{u} + (\nabla \mathbf{u})^\top \right)$ is the stress tensor, with the pressure p , the density ρ and the dynamic viscosity μ . The

only forces considered are the ST force at the interface denoted \mathbf{F}_Γ and the body force due the gravitational acceleration \mathbf{g} . Section 2.5 describes the formulation of the ST force. Without loss of generality, the imposed boundary conditions on $\partial\Omega$ are no-slip conditions.

Weak form. The weak form for p and \mathbf{u} is obtained using the corresponding test functions q and \mathbf{v} . The formulation includes stabilization terms to have a well-posed problem. Uniqueness of the solution is ensured using Pressure-Stabilizing/Petrov-Galerkin (PSPG) stabilization, which enable the use of same order elements for \mathbf{u} and p . Additionally, it includes the Streamline-Upwind/Petrov-Galerkin (SUPG) stabilization [22] to avoid oscillations in advection-dominated problems.

The solution and test spaces are [22]:

$$\mathcal{U} := \{\mathbf{u} \in H^1(\Omega)^D : \mathbf{u} = \mathbf{0} \text{ on } \partial\Omega\} \quad (3a)$$

$$\mathcal{V} := \{\mathbf{v} \in H^1(\Omega)^D : \mathbf{v} = \mathbf{0} \text{ on } \partial\Omega\} \quad (3b)$$

$$\mathcal{P} := \{p \in L^2(\Omega)\} \quad (3c)$$

$$\mathcal{Q} := \{q \in L^2(\Omega)\} \quad (3d)$$

where D denotes the spatial dimension. The complete weak problem is:

Find $p \in \mathcal{P} \times [0, t_{\text{end}}]$ and $\mathbf{u} \in \mathcal{U} \times (0, t_{\text{end}}]$, such that:

$$(q, \nabla \cdot \mathbf{u})_\Omega + \underbrace{(\tau_{u,k} \nabla q, \mathcal{R}_u)_{\Omega_k}}_{\text{PSPG}} = 0 \quad \forall q \in \mathcal{Q} \times (0, t_{\text{end}}] \quad (4)$$

$$\begin{aligned} \rho \left(\mathbf{v}, \frac{\partial \mathbf{u}}{\partial t} \right)_\Omega + \rho (\mathbf{v}, (\mathbf{u} \cdot \nabla) \mathbf{u})_\Omega - (\nabla \cdot \mathbf{v}, p)_\Omega + \mu \left(\nabla \mathbf{v}, (\nabla \mathbf{u} + (\nabla \mathbf{u})^\top) \right)_\Omega \\ + \underbrace{(\tau_{u,k} (\mathbf{u} \cdot \nabla) \mathbf{v}, \mathcal{R}_u)_{\Omega_k}}_{\text{SUPG}} = (\mathbf{v}, \mathbf{F}_\Gamma + \rho \mathbf{g})_\Omega \quad \forall \mathbf{v} \in \mathcal{V} \times (0, t_{\text{end}}] \quad (5) \end{aligned}$$

where \mathcal{R}_u is the strong residual of the momentum equation,

$$\mathcal{R}_u = \rho \left(\frac{\partial \mathbf{u}}{\partial t} + (\mathbf{u} \cdot \nabla) \mathbf{u} \right) - \nabla \cdot \boldsymbol{\sigma} - \mathbf{F}_\Gamma - \rho \mathbf{g} \quad (6)$$

and $\tau_{u,k}$ is a stabilization parameter. For transient problems, it takes the form [22, 23]:

$$\tau_{u,k} = \left[\left(\frac{1}{\Delta t} \right)^2 + \left(\frac{2\|\mathbf{u}_k\|n_p}{h_k} \right)^2 + 9 \left(\frac{4\nu n_p^2}{h_k^2} \right)^2 \right]^{-1/2} \quad (7)$$

where Δt is the time step, $\nu = \mu/\rho$ is the kinematic viscosity, $\|\mathbf{u}_k\|$ is the Euclidean norm of the cell velocity vector \mathbf{u}_k , and n_p is the degree of the polynomial approximation. h_k denotes the diameter of a disk (2D) or a sphere (3D) of the same area (2D) or volume (3D) as the element k :

$$h_{k,2D} = \sqrt{\frac{4V_k}{\pi}} , \quad h_{k,3D} = \left(\frac{6V_k}{\pi} \right)^{\frac{1}{3}} \quad (8)$$

where V_k is the area in 2D or volume in 3D of the element k . The current work uses Lagrange tensor product elements Q_m of degree $m = 1$ for \mathbf{u} and p .

2.2. Phase Indicator Transport

The framework defines the phase indicator as:

$$\phi(\mathbf{x}) = \begin{cases} 0 & \forall \mathbf{x} \in \Omega_0 \\ 1 & \forall \mathbf{x} \in \Omega_1 \end{cases} \quad (9)$$

with the interface $\Gamma := \{\mathbf{x} \in \Omega \mid \phi(\mathbf{x}) = 0.5\}$. The *strong form* of the problem for the transport of ϕ is:

$$\frac{\partial \phi}{\partial t} + \mathbf{u} \cdot \nabla \phi = 0 \quad \forall \mathbf{x} \in \Omega \times (0, t_{\text{end}}] \quad (10)$$

Without loss of generality, Dirichlet boundary conditions are considered such that:

$$\phi(\mathbf{x}) = 0 \quad \forall \mathbf{x} \in \partial\Omega \quad (11)$$

Weak form. The weak form uses the scalar test function s and includes SUPG stabilization due to the pure-advection form of Equation (10).

The solution and test spaces are:

$$\Phi := \{\phi \in H^1(\Omega) : \phi = 0 \text{ on } \partial\Omega\} \quad (12)$$

$$\mathcal{S} := \{s \in H^1(\Omega) : s = 0 \text{ on } \partial\Omega\} \quad (13)$$

respectively. The problem reads:

Find $\phi \in \Phi \times [0, t_{\text{end}}]$ such that

$$\left(s, \frac{\partial \phi}{\partial t} + \mathbf{u} \cdot \nabla \phi \right)_{\Omega} + \underbrace{(\tau_{\phi,k} (\mathbf{u} \cdot \nabla s), \mathcal{R}_{\phi})_{\Omega_k}}_{\text{SUPG}} = 0 \quad \forall s \in \mathcal{S} \times (0, t_{\text{end}}] \quad (14)$$

where \mathcal{R}_{ϕ} is the strong residual of Equation (10), $\mathcal{R}_{\phi} = \frac{\partial \phi}{\partial t} + \mathbf{u} \cdot \nabla \phi$, and $\tau_{\phi,k}$ is a stabilization parameter defined by Tezduyar [23]:

$$\tau_{\phi,k} = \left[\left(\frac{1}{\Delta t} \right)^2 + \left(\frac{2\|\mathbf{u}_k\|}{h_k} \right)^2 \right]^{-1/2} \quad (15)$$

The current work uses Q_m elements of degree $m = 1$ for ϕ .

2.3. Time Integration and Equations Coupling

An implicit Backward Differentiation Formula of order 2 (BDF2) discretizes the transient terms of Equations (5) and (14).

The framework explicitly treats the coupling between the NS equations and the phase indicator transport, which occurs through the velocity \mathbf{u} , the physical properties ($\rho(\phi)$ and $\mu(\phi)$), and the ST term ($\mathbf{F}_{\Gamma}(\phi)$). For a given time iteration $n + 1$, corresponding to the time $t + \Delta t$, the framework:

1. solves the phase indicator advection (14) for ϕ^{n+1} using an approximation of the velocity $\hat{\mathbf{u}}^{n+1}$ computed from a linear extrapolation of the two previous solutions, \mathbf{u}^n and \mathbf{u}^{n-1} ,
2. performs the reinitialization of ϕ^{n+1} if the time iteration $n + 1$ is a reinitialization time step, and,
3. solves the monolithic formulation of the fluid dynamics system formed by Equations (4) and (5) for \mathbf{u}^{n+1} and p^{n+1} , with $\rho(\phi^{n+1})$, $\mu(\phi^{n+1})$, and $\mathbf{F}_\Gamma(\phi^{n+1})$.

2.4. Physical Properties

The change of any given physical property λ at the interface follows [8]:

$$\lambda = \lambda_0 \hat{H}_\Gamma(\mathbf{x}) + \lambda_1 (1 - \hat{H}_\Gamma(\mathbf{x})) \quad (16)$$

where λ_i , with $i \in \{0, 1\}$, is the value of the property in Ω_i . $\hat{H}_\Gamma(\mathbf{x})$ is the approximation of the Heaviside function stepping at the interface:

$$\hat{H}_\Gamma(\mathbf{x}) = 0.5 \tanh [\beta (\phi(\mathbf{x}) - 0.5)] + 0.5 \quad (17)$$

where β is a model parameter that controls the sharpness of the phase transition.

2.5. Surface Tension Force

The volumetric formulation of the ST force in Equation (2) is:

$$\mathbf{F}_\Gamma = \underbrace{(-\gamma \kappa \mathbf{n})}_{\substack{\text{Normal} \\ \text{force}}} + \underbrace{\nabla_\Gamma \gamma}_{\substack{\text{Tangential} \\ \text{force}}} \|\nabla \hat{H}_\Gamma\| \quad (18)$$

where γ is the ST coefficient, κ is the curvature, \mathbf{n} is the unit normal vector of the interface pointing away from Ω_0 . ∇_Γ represents the orthogonal projection

of ∇ on Γ . $\|\nabla \hat{H}_\Gamma\|$ is the approximation of the Dirac Delta distribution with a support on the interface proposed in the Continuous Surface Force (CSF) model by Brackbill et al. [24].

This work considers a linear variation of the ST coefficient γ to a given scalar field $G(\mathbf{x})$:

$$\gamma(\mathbf{x}) = \gamma_0 + \gamma' (G(\mathbf{x}) - G_0) \quad (19)$$

where γ_0 is the reference ST coefficient at the reference scalar value G_0 and γ' is the constant rate of change of γ with respect to $G(\mathbf{x})$. For example, if thermo-capillarity is considered, $G(\mathbf{x})$ would represent the temperature field.

With this definition of $\gamma(\mathbf{x})$, Equation (18) takes the form:

$$\mathbf{F}_\Gamma = [-\gamma \kappa \mathbf{n} + \gamma' (\nabla G - \mathbf{n} (\mathbf{n} \cdot \nabla G))] \|\nabla \hat{H}_\Gamma\| \quad (20)$$

2.6. Normal and Curvature Computations

The normal \mathbf{n} and curvature κ terms in Equation (18) are respectively:

$$\mathbf{n} = \frac{\nabla \phi}{\|\nabla \phi\|} \quad (21)$$

$$\kappa = \nabla \cdot \mathbf{n} \quad (22)$$

The finite element approximation ϕ_h is in the approximation space \mathcal{S}_h , for which the basis functions are constructed using Lagrange Q_m polynomials. The current framework typically uses Q_1 elements. It results in $\kappa \notin \mathcal{S}_h$ since it involves the second derivatives of ϕ_h .

For this reason, instead of computing the interface normal vector field with Equation (21) and the curvature with Equation (22), the solver computes their \mathcal{L}^2 projections to ensure $\kappa \in \mathcal{S}_h$ using the approach proposed by Zahedi et al. [25]

Considering an arbitrary vector function on the domain $\boldsymbol{\nu} \in \mathcal{L}^2(\Omega)^D$ as the test function, the following problem is considered for the projection of the regularized phase fraction gradient $\boldsymbol{\zeta}$:

Find $\boldsymbol{\zeta} \in \mathcal{L}^2(\Omega)^D$ such that

$$(\boldsymbol{\nu}, \boldsymbol{\zeta})_\Omega + (\nabla \boldsymbol{\nu}, \eta_\zeta \nabla \boldsymbol{\zeta})_\Omega = (\boldsymbol{\nu}, \nabla \phi)_\Omega \quad \forall \boldsymbol{\nu} \in \mathcal{L}^2(\Omega)^D \quad (23)$$

where $\eta_\zeta = ah^2$ is the normal filter with a a constant usually set to 4. Following Equation (21), the normal vector approximation is:

$$\boldsymbol{n} \approx \hat{\boldsymbol{n}} = \frac{\boldsymbol{\zeta}}{\|\boldsymbol{\zeta}\|} \quad (24)$$

The projected curvature $\hat{\kappa}$ is computed by solving the following problem:

Find $\hat{\kappa} \in \mathcal{L}^2(\Omega)$ such that

$$(K, \hat{\kappa})_\Omega + (\nabla K, \eta_{\hat{\kappa}} \nabla \hat{\kappa})_\Omega = (\nabla K, \hat{\boldsymbol{n}})_\Omega \quad \forall K \in \mathcal{L}^2(\Omega) \quad (25)$$

Here, $K \in \mathcal{L}^2(\Omega)$ is the arbitrary scalar test function and $\eta_{\hat{\kappa}} = bh^2$ is the curvature filter with b a constant usually set to 1. The framework uses Q_m elements with the same degree as the phase indicator to approximate the normal and curvature.

2.7. Software

Lethe, an open-source CFD software framework based on the **deal.II** finite element library [26], implements the current work. It is a fully-parallel, multi-phase and multi-physics solver and uses FEM with a CG formulation. It considers Lagrange tensor product elements (Q_m) of arbitrary degree m (quadrilaterals in 2D and hexahedra in 3D). It features adaptive mesh refinement capabilities using the **p4est** library [27]. A thorough description of **Lethe** is available in [22].

`Lethe` estimates the error for the mesh adaptation using Kelly's error estimator [28]. It performs refinement and coarsening by estimating the error via the jump in the gradient between the faces for a selected variable. For the interfacial problems targeted in the current work, selecting the variable ϕ enables local refinement around the interface.

3. Interface Reinitialization Methods

The complete formulation of the problem presented in the last sections does not include any self-sharpening features to avoid smearing of the interface. Mesh adaptation only reduces numerical diffusion of the interface without completely removing it.

Hence, the current framework relies on reinitialization methods to maintain a constant interface thickness and reduce the regularization error discussed in Section 1. This work considers three methods: PDE-based reinitialization, geometric reinitialization, and projection-based reinitialization. The frequency of the reinitialization is $f = 1/(N_{\text{reinit}}\Delta t)$, where N_{reinit} indicates the number of time steps between reinitialization steps.

3.1. PDE-Based Reinitialization

This work studies the PDE-based reinitialization method proposed by Olsson et al. [6]. It solves the following PDE in an artificial time until reaching steady-state:

$$\underbrace{\frac{\partial \phi_{\text{reinit}}}{\partial \tau}}_{\text{transient}} + \underbrace{\nabla \cdot [\phi_{\text{reinit}}(1 - \phi_{\text{reinit}})\mathbf{n}]}_{\text{compression}} - \underbrace{\varepsilon \nabla \cdot [(\nabla \phi_{\text{reinit}} \cdot \mathbf{n})\mathbf{n}]}_{\text{diffusion}} = 0 \quad (26)$$

where τ is the artificial time and ε is a diffusion coefficient. The solution corresponds to the quasi-steady balance between the compressive and diffusive

terms and the interface takes the form of a hyperbolic tangent profile along its thickness [7, 8, 29]:

$$\phi_{\text{reinit}}(\mathbf{x}) = 0.5 - 0.5 \tanh\left(\frac{d(\mathbf{x})}{2\varepsilon}\right) \quad (27)$$

where $d(\mathbf{x})$ is the signed-distance function from the interface. The choice of the diffusion coefficient ε determines the interface thickness.

Steady-state. In the current numerical framework, Equation (26) reaches steady-state when one of the two following stopping criteria is met¹:

Criterion I.

$$\alpha_{\text{steady-state}} \geq \frac{\|\phi_{\text{reinit}}^{\iota+1} - \phi_{\text{reinit}}^{\iota}\|}{\|\phi_{\text{reinit}}^{\iota}\|}$$

where $\alpha_{\text{steady-state}}$ is a user-defined steady-state tolerance (set to 10^{-4} in this work), and ι represents an artificial time iteration.

Criterion II.

$$\iota \geq N_{\tau}$$

where N_{τ} is a user-defined maximum number of artificial time iterations.

Figure 2 summarizes the steps of the PDE-based reinitialization process. Once the reinitialized phase indicator field replaces the initial phase indicator field (end of Figure 2), the solver recomputes the normal vector field with Equation (24) and the curvature field with Equation (25). Finally, the solution of the NS momentum Equation (5) uses these new solution fields.

¹Note that the solver uses an implicit BDF1 time-integration scheme for the PDE-based reinitialization since the objective is to reach a steady-state solution and the temporal accuracy of the artificial time-stepping method is not important [6].

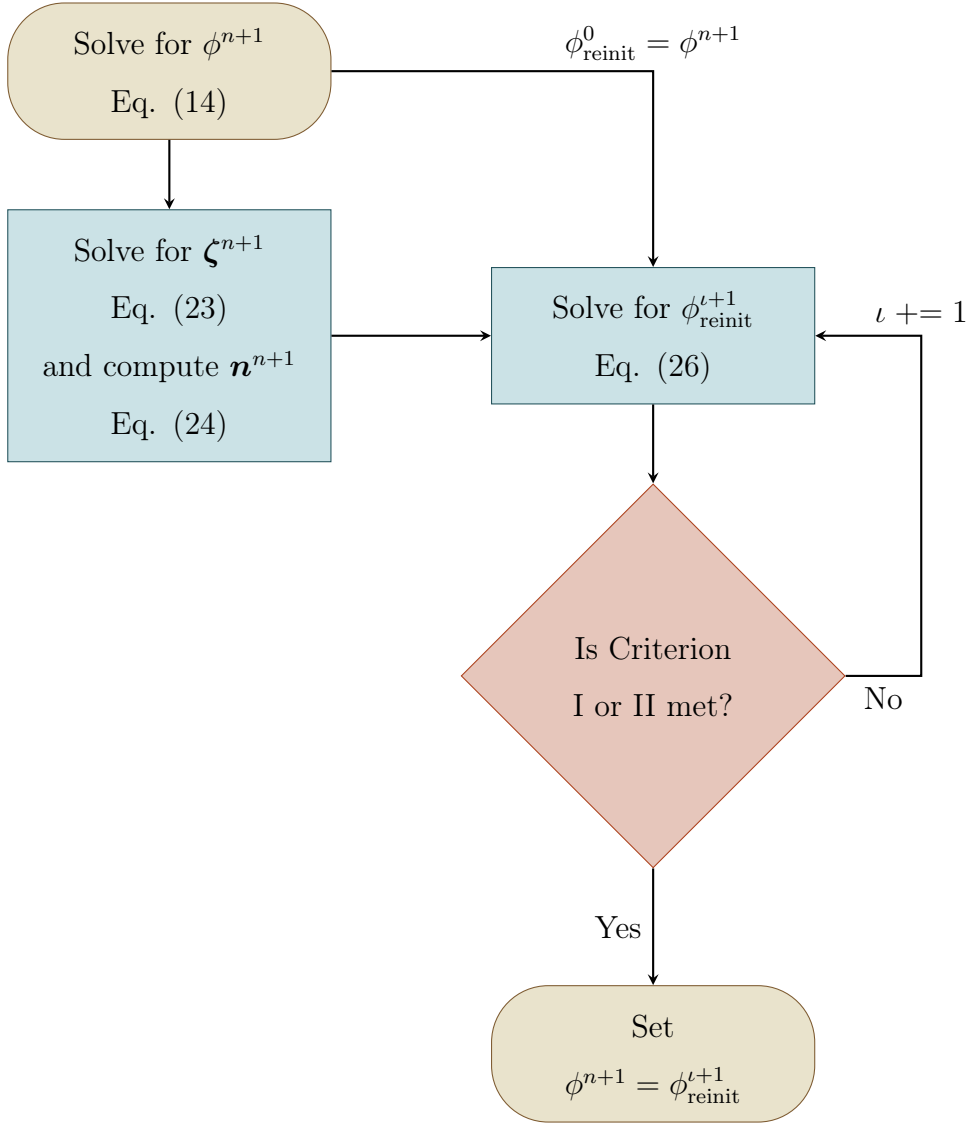


Figure 2: PDE-based reinitialization process flow diagram

3.2. Geometric reinitialization

This work proposes a new geometric reinitialization approach based on the method of Mut et al. [30] and Ausas et al. [13] developed in the context of LS frameworks. The reinitialization method uses the following property

of signed distance functions [30], illustrated in Figure 3:

Let \mathcal{C} be a surface of \mathbb{R}^D dividing the latter into two open domains Ω^+ and Ω^- such that $\Gamma \subset \Omega^-$. Then,

$$|d(\mathbf{y})| = \min_{\mathbf{x} \in \mathcal{C}} (\|\mathbf{y} - \mathbf{x}\| + |d(\mathbf{x})|) \quad \forall \mathbf{y} \in \Omega^+ \quad (28)$$

where $d(\mathbf{x})$ is a signed distance function:

$$d(\mathbf{x}) = S(\mathbf{x}) \min_{\mathbf{c} \in \Gamma} \|\mathbf{x} - \mathbf{c}\| \quad (29)$$

with \mathbf{c} , the closest point of \mathbf{x} on Γ , and

$$S(\mathbf{x}) = \begin{cases} -1 & \forall \mathbf{x} \in \Omega_1 \\ 1 & \forall \mathbf{x} \in \Omega_0 \end{cases} \quad (30)$$

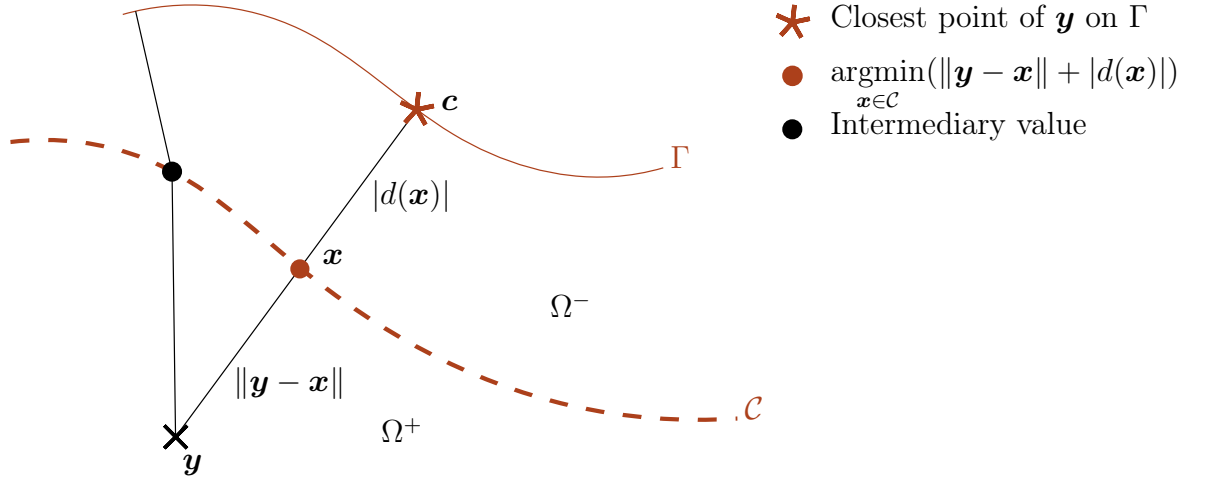


Figure 3: Distance property described in Equation (28).

In other words, the property states that the minimal distance of a given point \mathbf{y} to Γ can be computed using the knowledge of the distance function on an intermediary surface \mathcal{C} .

In a discrete frame, the implementation of the geometric method consists of three steps, as illustrated in the flow diagram of Figure 4:

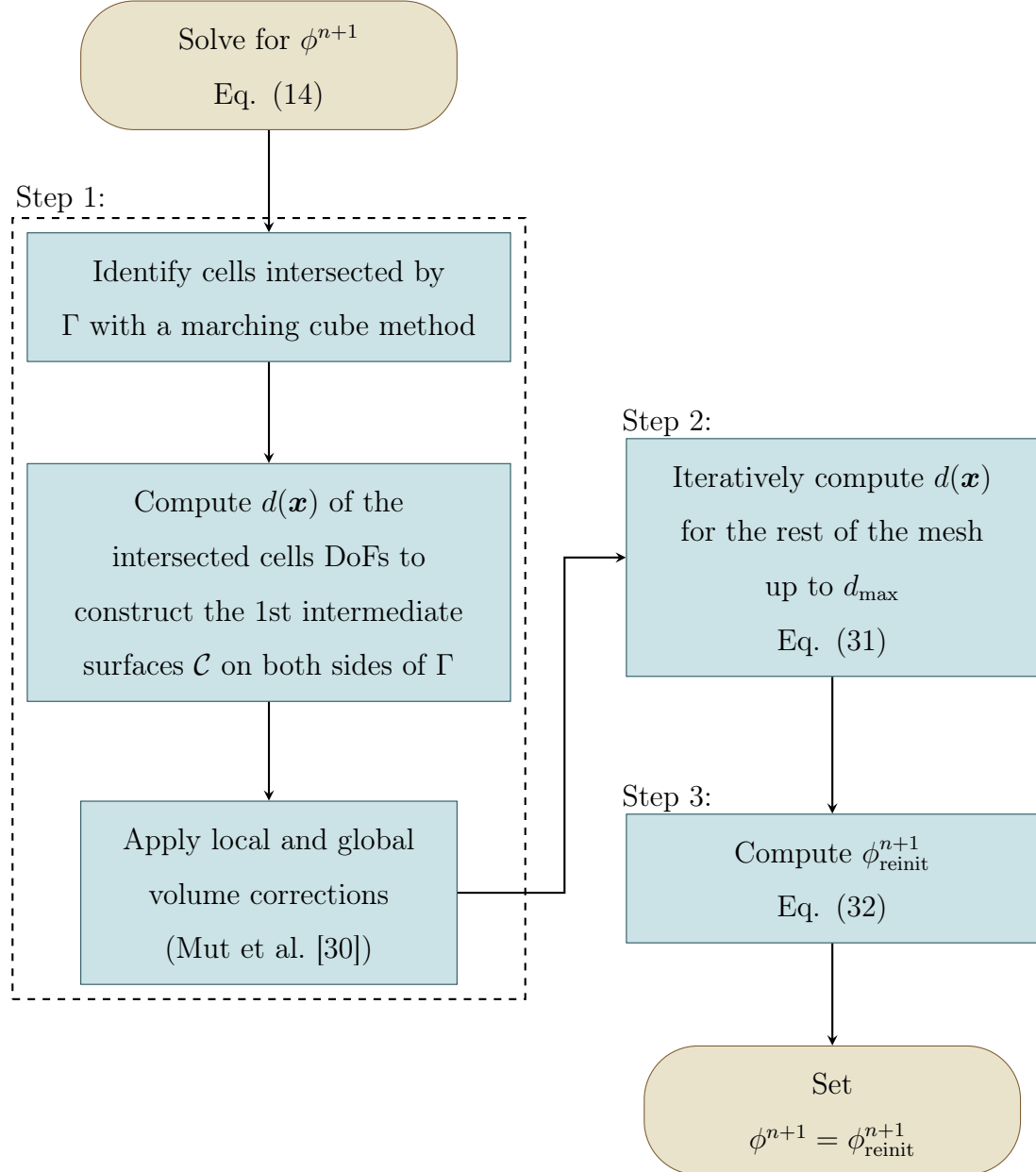


Figure 4: Geometric reinitialization flow diagram

Step 1: First Intermediary Surface. The method reconstructs the interface Γ in each intersected cell into linear segments in 2D and planar elements in 3D from the iso-contour $\phi = 0.5$ using a marching cube method.

It builds the first intermediary surface \mathcal{C} on each side of the interface by computing the distance between the interface reconstruction and the DoFs of the intersected cells. In 2D, it corresponds to point-to-line-segment distance computation, and in 3D, to point-to-plane distance computation.

The method of Mut et al. [30] also includes a volume correction step to account for volume loss/gain introduced by the signed distance function not being part of the Lagrange polynomial space ($d(\mathbf{x}) \notin Q_m$). It corrects the DoF values of the intersected cells to conserve cell-wise and global volumes; the reader can refer to [30] for more details on the volume conservation algorithm.

Step 2: Distance Computation of the Rest of the Mesh. With the knowledge of $d(\mathbf{x})$ on the first surface \mathcal{C} , the approach computes the distance for the rest of the mesh up to a user-defined maximum distance d_{\max} . It builds successive surfaces \mathcal{C} by resolving the following minimization problem for each DoF i of a cell, as illustrated in Figure 5:

$$|d(\mathbf{y}_i)| = \min_{\mathbf{x} \in \mathcal{F}_j} (\|\mathbf{y}_i - \mathbf{x}\| + |d(\mathbf{x})|) \quad (31)$$

where \mathbf{y}_i is the coordinate of the DoF i , \mathcal{F}_j is a face opposite to the DoF i , and \mathbf{x} is a point on \mathcal{F}_j . Equation (31) corresponds to Equation (28) in a discrete frame, hence, \mathcal{F}_j is the counterpart of \mathcal{C} .

It is an iterative approach similar to a marching method: it solves equation (31) for each DoF of each cell until $d(\mathbf{y}_i)$ converges.

The main differences between the current framework and the original works of Mut et al. [30] and Ausas et al. [13] is highlighted in Figure 5: the proposed approach is suitable for quadrilateral/hexahedral elements and adaptively refined grids. The adaptation to quadrilateral/hexahedral lies in the treatment of multiple opposite faces instead of only one. For the adaptively refined grids, the method treats the coarse and refined cells in the same way. The only requirement is to constraint the distance value at the hanging nodes to ensure continuity of the distance field, as typically done in dynamic mesh adaptation [31]. The proposed method applies this constrain upon convergence of the iterative loop. Finally, the method works in a distributed parallel framework, which Mut et al. [30] and Ausas et al. [13] do not discuss in their works.

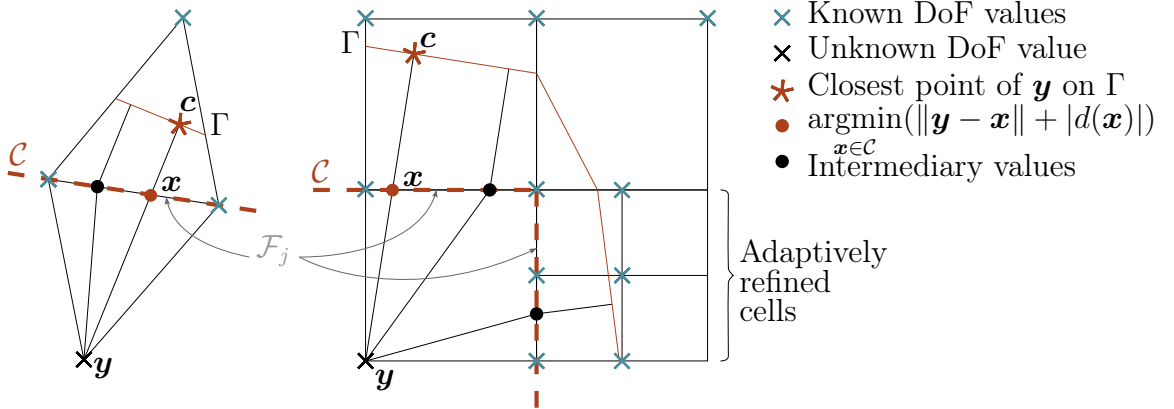


Figure 5: Geometric redistanciation for quadrilateral and adaptively refined (right) meshes compared to the method of Mut et al. [30] and Ausas et al. [13] for simplex meshes (left).

Step 3: Phase Indicator Computation. The last step is to convert the signed distance field to a phase indicator using a tanh-based transformation:

$$\phi_{\text{reinit}}(\mathbf{x}) = 0.5 - 0.5 \tanh\left(\frac{d(\mathbf{x})}{2\varepsilon}\right) \quad (32)$$

where ε is a measure of the interface thickness. This transformation ensures a smooth transition of the phase indicator, which is numerically desirable to solve Equation (14). It imposes $\phi_{\text{reinit}}(\mathbf{x}) = 0.5$ when $d(\mathbf{x}) = 0$, however it does not strongly impose the extrema $\phi_{\text{reinit}}(\mathbf{x}) = 0$ or 1 away from Γ and their values depend on d_{\max} . It has no significant impact on the results.

3.3. Projection-Based Reinitialization

The projection-based reinitialization is the simplest of all three reinitialization methods discussed in this article. It projects the phase indicator to a sharper space. The current work studies the method proposed by Aliabadi and Tezduyar [10] in which the reinitialized phase indicator is given by:

$$\phi_{\text{reinit}} = \begin{cases} c^{1-\alpha} \phi^\alpha & \text{if } 0 \leq \phi \leq c \\ 1 - (1-c)^{1-\alpha} (1-\phi)^\alpha & \text{if } c \leq \phi \leq 1 \end{cases} \quad (33)$$

where c corresponds to the iso-level $\phi = c$ for which the volume is conserved and α is the interface sharpening parameter. The value of c can be obtained from a volume-conservation routine, as described by Aliabadi and Tezduyar [10]. The current work, fixes it to 0.5 from the observation that any other values result in a global displacement of the interface. The interface sharpening parameter $\alpha = 1.5$ is selected and corresponds to the value proposed by Aliabadi and Tezduyar [10].

3.4. Summary and Parameters

Table 1 presents a summary of the three methods, highlighting their parameters and the solution profile of the phase indicator in the normal direction of the interface. It shows that the solution of the PDE-based and geometric reinitialization are the same, with ε controlling the thickness of the interface.

Table 1: Reinitialization methods summary

Method	Solution profile	Parameters
PDE-based	$0.5 - 0.5 \tanh(d(\mathbf{x})/(2\varepsilon))$	$\varepsilon, \Delta\tau, \alpha_{\text{steady-state}}, N_\tau$
Geometric	$0.5 - 0.5 \tanh(d(\mathbf{x})/(2\varepsilon))$	ε, d_{\max}
Projection-based	Piece-wise form given by Equation (33)	c, α

4. Results

This section assesses the effects of the reinitialization methods by comparing their respective results on relevant benchmarks. It also includes a sensitivity study to the reinitialization frequency $1/(N_{\text{reinit}}\Delta t)$.

The rising bubble benchmark and the capillary migration cases use $\{\mathbb{M}\mathbb{L}\mathbb{T}\}$ dimensions to describe the domain sizes and the physical properties, where \mathbb{M} stands for mass, \mathbb{L} for length, and \mathbb{T} for time units. Table 2 reports the simulation parameters for the three cases.

4.1. Rising Bubble Benchmark

The rising bubble benchmark originates from the work of Hysing et al. [18] in 2D. The current application case focuses on the 3D extension of the benchmark proposed by Adelsberger et al. [32].

4.1.1. Description of the Case

The benchmark simulates an incompressible bubble of radius $R = 0.25\mathbb{L}$ rising in the center of a cuboid column due to buoyancy, as illustrated in Figure 6.

The selected set of physical properties follows the one proposed by Adelsberger et al. [32], denoted Case 1 in the reference work. Table 3 lists them along with the two relevant dimensionless numbers: the Reynolds number $\text{Re} = \rho_0 U_g D_b / \mu_0$ and the Eötvös number $\text{Eo} = \rho_0 U_g^2 D_b / \gamma$, where $U_g = \sqrt{g D_b}$ is the reference velocity and $D_b = 2R$ is the diameter of the bubble.

The problem formulation imposes all walls to no-slip conditions for the NS equations [19, 32] and no-flux for the phase indicator transport. Both

Table 2: General and specific parameters for the three cases. RB, CM, and RP stand for Rising Bubble, Capillary Migration and Rayleigh-Plateau, respectively. Cartesian grids discretize the domain of each case, with h being the side length of the smallest cell.

General simulation parameters				
Parameters	Dimensions	RB	CM	RP
Regularization sharpness β	-	20	20	20*
Normal projection factor a	-	4	4	4
Curvature projection factor b	-	1	1	1
Mesh adaptation frequency	\mathbb{T}^{-1}	$1/(5\Delta t)$	$1/(20\Delta t)$	$1/(10\Delta t)$
PDE-based reinitialization				
Parameters	Dimensions	RB	CM	RP
Interface thickness measure ε	\mathbb{L}	h	$2h$	h
Artificial time step $\Delta\tau$	\mathbb{T}	Δt	Δt	Δt
Steady-state criterion $\alpha_{\text{steady-state}}$	-	1×10^{-4}	1×10^{-4}	1×10^{-4}
Max. number of artificial time step N_τ	-	10 000	10 000	10 000
Geometric reinitialization				
Parameters	Dimensions	RB	CM	RP
Interface thickness measure ε	\mathbb{L}	$3h$	$3h$	$3h$
Max. redistanciation distance d_{\max}	\mathbb{L}	8ε	8ε	4ε
Projection-based reinitialization				
Parameters	Dimensions	RB	CM	RP
Iso-level c	-	0.5	0.5	0.5
Interface sharpening parameter α	-	1.5	1.5	1.5
Initial interface thickness measure ε	\mathbb{L}	$3h$	$3h$	$3h$

* The Rayleigh-Plateau case deactivates the approximation \hat{H}_Γ described by Equation (17) for the PDE-based method, else poor volume conservation and slower spacial convergence rates are observed.

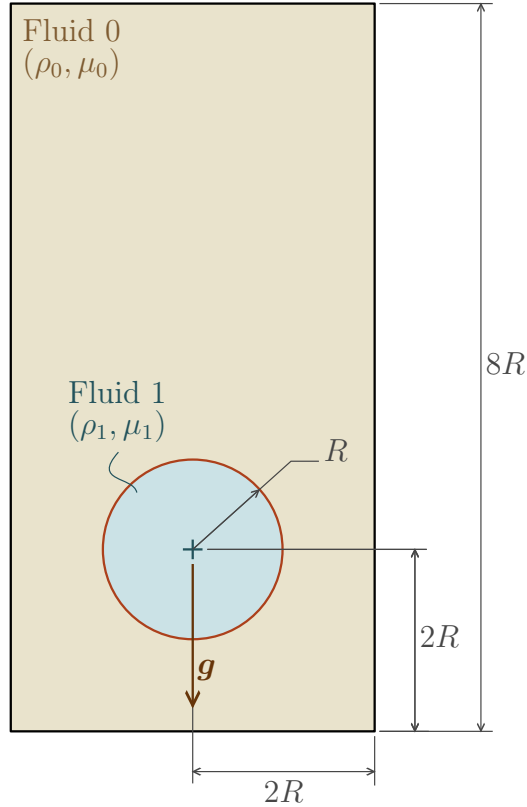


Figure 6: 2D cross-section view in the x-y plane of the initial state of the rising bubble case

fluids are initially at rest. The phase indicator initial condition is:

$$\phi_0(\mathbf{x}) = 0.5 - 0.5 \tanh\left(\frac{d_0(\mathbf{x})}{2\varepsilon}\right) \quad (34)$$

$$d_0(\mathbf{x}) = \|\mathbf{x} - \mathbf{x}_0\| - R \quad (35)$$

where d_0 is the signed distance function of a sphere of radius R centered at \mathbf{x}_0 according to Figure 6. The case considers a rising time of $3\mathbb{T}$.

Table 3: Physical properties of the rising bubble case

Parameters	Dimensions	Values
Reynolds number (Re)	-	35
Eötvös number (Eo)	-	10
Density ratio (ρ_0/ρ_1)	-	10
Density of fluid 0 (ρ_0)	ML^{-3}	1000
Viscosity ratio (μ_0/μ_1)	-	10
Dynamic viscosity of fluid 0 (μ_0)	$\text{ML}^{-1}\text{T}^{-1}$	10
ST coefficient (γ)	MT^{-2}	24.5
Gravitational acceleration magnitude (g)	LT^{-2}	0.98

4.1.2. Metrics of Interest

The metrics of interest are the barycenter height and the rise velocity along the rising axis (y -axis), based on the benchmark of Adelsberger et al. [32]. The current work considers the following definitions:

$$\text{Barycenter height} = \frac{\int_{\Omega} y \hat{H}_{\Gamma} d\Omega}{\int_{\Omega} \hat{H}_{\Gamma} d\Omega} \quad (36)$$

$$\text{Rise velocity} = \frac{\int_{\Omega} u_y \hat{H}_{\Gamma} d\Omega}{\int_{\Omega} \hat{H}_{\Gamma} d\Omega} \quad (37)$$

where u_y is the y component of the velocity vector \mathbf{u} . The rise velocity corresponds to the mean velocity in the y direction inside the bubble.

This case also monitors the relative volume evolution V/V_0 and the spheric-

ity A_{eq}/A_{Γ} of the bubble, computed according to:

$$\frac{V}{V_0} = \frac{\int_{\Omega_1} d\Omega}{\int_{\Omega_1} d\Omega \Big|_{t=0}} \quad (38)$$

$$\frac{A_{\text{eq}}}{A_{\Gamma}} = \frac{\pi^{\frac{1}{3}} (6V)^{\frac{2}{3}}}{\int_{\Gamma} dS} \quad (39)$$

where V is the volume at the time t , V_0 is the initial volume, A_{eq} is the area of a sphere with a volume equivalent to V and $A_{\Gamma} = \int_{\Gamma} dS$ is the surface area of the bubble. The solver approximates the latter using a Gauss-Legendre quadrature rule with 2 points in each direction on the iso-contour $\phi = 0.5$.

The work of Adelsberger et al. [32] provides reference solutions for the barycenter height, rise velocity, and sphericity from three different solvers: DROPS, NaSt3DGP, and OpenFoam. Turek et al. [19] also report simulation results of the solver FeatFlow for the rise velocity and sphericity. Table 4 presents a summary of the methods used in the reference solvers.

Table 4: Reference solvers specifications for the rising bubble case

Developer	Spatial discretization	Time discretization	Interface solver	STF modeling	Reinitialization method
DROPS [32, 33, 34]	Institute of Geometry and Applied Mathematics (IGPM), RWTH Aachen	XFEM	Implicit θ -scheme	- CSF - Curvature approximated with weak formulation of Laplace-Beltrami-Operator	Fast-marching method
FeatFlow [19, 35]	Institute of Applied Mathematics (Chair III), TU Dortmund	FEM	Not specified	- Semi-implicit treatment - Laplace-Beltrami transformation	Not specified
NaSt3DGF [32, 36, 37]	Institute for Numerical Simulation (INS), University of Bonn	Finite differences	2nd order Adams-Basforth scheme	CSF	PDE-based
OpenFOAM [32, 38]	Multiple contributors (open source)	Finite volumes	Implicit Euler scheme	VOF CSF	None

4.1.3. Simulation Settings

For each reinitialization method, the study investigates three reinitialization frequencies: $f = 1/(N_{\text{reinit}}\Delta t)$, with $N_{\text{reinit}} \in \{1, 10, 100\}$.

An adaptively refined Cartesian grid discretizes the domain. The minimum and maximum element sizes are $7.81 \times 10^{-3}\mathbb{L}$ and $6.25 \times 10^{-2}\mathbb{L}$ respectively. The selected time step respects the capillary time step limit defined as [24]:

$$\Delta t_\gamma = \sqrt{\frac{(\rho_0 + \rho_1)h^3}{4\pi\gamma}} \quad (40)$$

where h is the minimum cell size, defined as the side length of the smallest cell in this work. For this case, it results in a constant time step of $\Delta t = 1.3 \times 10^{-3}\mathbb{T}$. Hence, the Courant-Friedrichs-Lowy condition (CFL) is not constant, and stabilizes at the end of the simulation at averaged values of 0.069, 0.082, and 0.075 for the PDE-based, geometric, and projection-based methods, respectively.

4.1.4. Results

Figures 7 to 11 present the final bubble shape, as well as the time evolution of the barycenter height, rise velocity, volume conservation, and sphericity. The results of PDE-based reinitialization, geometrical redistanciation, and projection-based reinitialization are respectively in purple, orange, and green. A darker shade of the color indicates a higher reinitialization frequency. The figures for the results use the same color scheme for all plots. The reference curves correspond to the results for the finest discretization reported in [19, 32].

Bubble shape and barycenter position. Figure 7 shows the bubble contour in the xy -plane at the end of the simulation time for each method.

For the PDE-based approach, the reinitialization frequency has no significant effect on the bubble shape and position: for all frequencies, the contours are superposed and follow a staircase pattern. The latter is caused by the choice of a small value of $\varepsilon = h$. The evolution of the barycenter height showed in Figure 8 agrees well the reference results of DROPS and NaStDGPF.

The geometric redistanciation method leads to the same results quality as the PDE-based approach. However, the shape is smoother than the PDE-based results since the selected value of $\varepsilon = 3h$ is larger.

The projection-based method shows the strongest effect of the frequency on all the metrics of interest. Only the results for the frequencies of $1/(10\Delta t)$ and $1/(100\Delta t)$ are presented because the solver fails with a reinitialization frequency of $1/\Delta t$. The bubble contours in Figure 7 show a strong staircase pattern for both frequencies, with significant differences in size and position. The corresponding barycenter evolution presented in Figure 8 for $f = 1/(10\Delta t)$ is not comparable to the reference curves, while the results for $f = 1/(100\Delta t)$ are in better agreement.

Rise velocity. Figure 9 shows the evolution in time of the rise velocity. For the PDE-based method and geometric approaches, the rise velocity evolution agrees well with the reference curves, especially to the ones of DROPS and NaSt3DGPF. There is no significant effect of the frequency. The projection-based results for the lowest frequency of $f = 1/(100\Delta t)$ are in better agreement with the reference values than the ones with a frequency of $1/(10\Delta t)$.

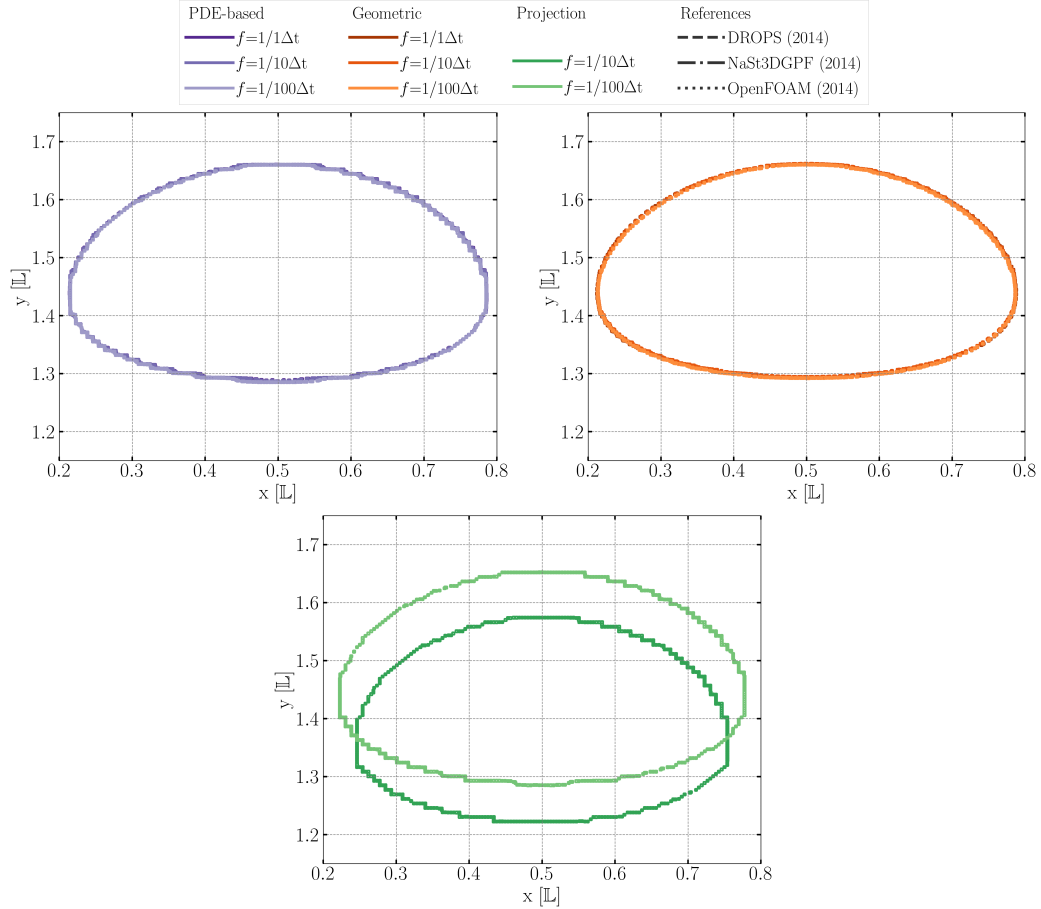


Figure 7: Comparison of the final bubble interface contours for different reinitialization methods at different reinitialization frequencies. The contours are extracted from the slice along the xy -plane passing by the center of the domain. On the upper panels, the PDE-based (left) and geometric (right) methods display very little influence of the reinitialization frequency. In contrast, on the lower panel, the projection-based method results in two significantly different bubble shapes.

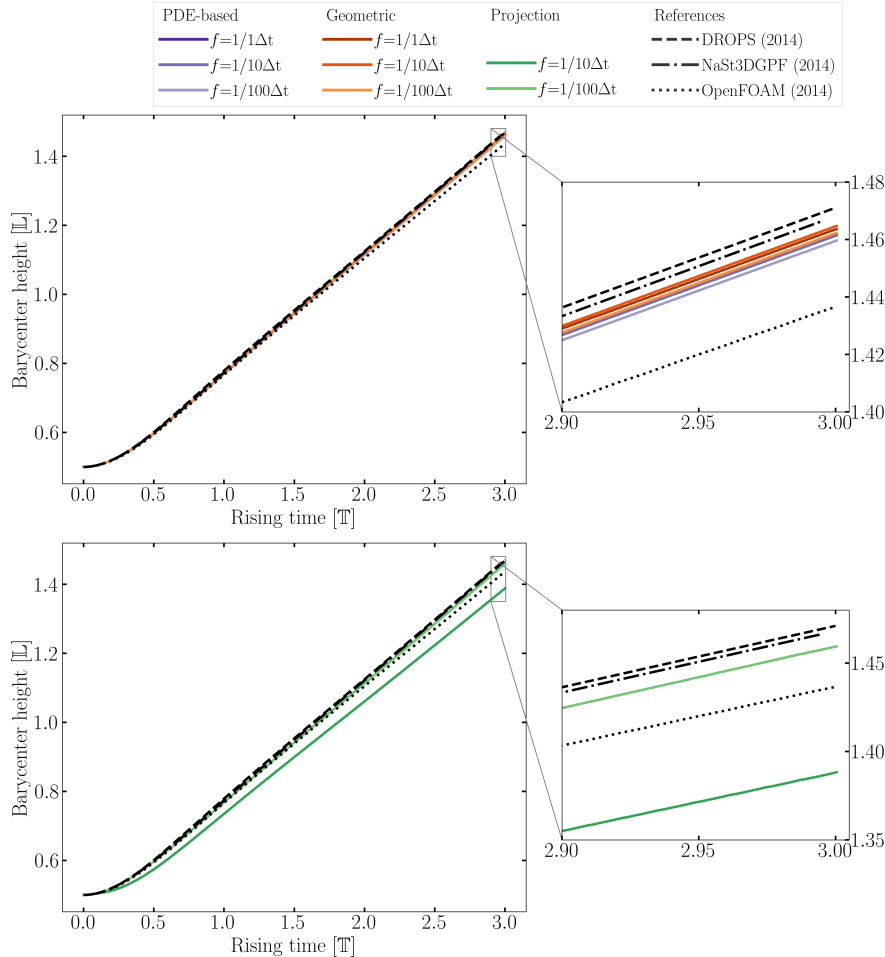


Figure 8: Comparison of the barycenter evolution for different reinitialization methods at different reinitialization frequencies with reference values [19, 32]. On the top panel, PDE-based and geometric methods capture trends similar to references (with the exception of OpenFOAM [32]). On bottom panel, projection-based results display a larger dependency to the reinitialization frequency.

Relative volume evolution. The relative volume evolution is presented in Figure 10. The PDE-based reinitialization results in a volume loss of less than 1% for $f = 1/(\Delta t)$. At the lowest frequency of $f = 1/(100\Delta t)$, the vol-

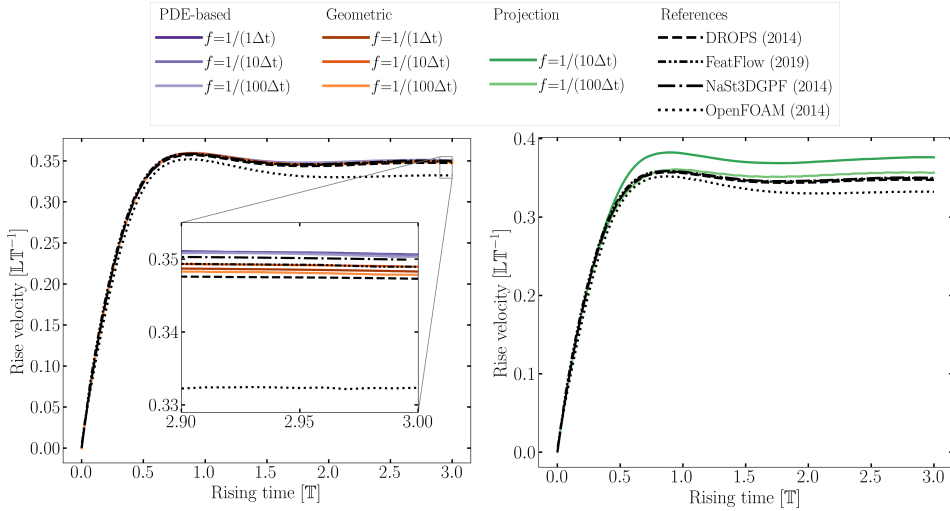


Figure 9: Comparison of the rise velocity for different reinitialization methods at different reinitialization frequencies with reference values [19, 32]. The PDE-based and geometric methods (left panel) capture similar trends to those of the references (with the exception of OpenFOAM [32]). In contrast, the projection based method (right panel), overestimates the rise velocity.

ume loss is approximately $\approx 1.5\%$. However, at this frequency, the evolution features jumps at regular time intervals corresponding to the application of the reinitialization. This variation in the volume indicates that the interface moves at each reinitialization step. For the geometric method, the relative volume evolution remains close to 1 for $f = 1/\Delta t$, while the results for $f \in \{1/(10\Delta t), 1/(100\Delta t)\}$ present a volume loss of up to approximately 2%. The projection-based results reveal a significant volume loss: the final bubble volume is approximately 75% of its initial volume for $f = 1/(10\Delta t)$ and 92% for $f = 1/(100\Delta t)$.

For all methods, there is no steady-state reached for the volume: it keeps decreasing for all frequencies, even when the rise velocity in Figure 9 reaches

a constant value. However, for the geometric method at $f = 1/\Delta t$, the rate of volume loss is significantly lower than all other methods.

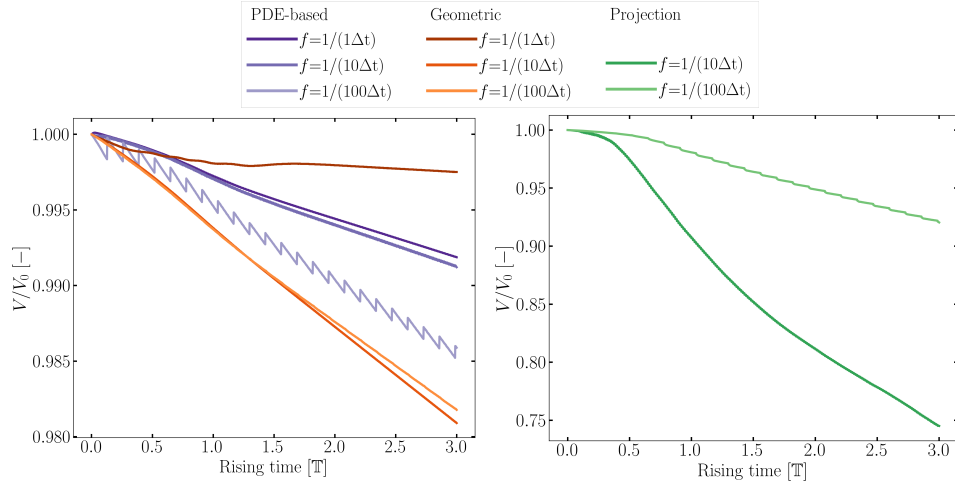


Figure 10: Comparison of relative geometrical volume evolution for different reinitialization methods at different reinitialization frequencies. On the left panel, PDE-based and geometric reinitialization methods show good volumetric conservation (under 2% loss). In contrast, projection-based reinitialization (right panel) displays poor volume conservation (more than 25% loss for the highest frequency).

Sphericity. Figure 11 shows the evolution in time of the sphericity. For the PDE-based method, the sphericity is higher than the reference values, indicating that the shape of the bubble is closer to a sphere. Additionally, it features jumps resulting from the reinitialization frequency of $f = 1/(100\Delta t)$. It also is consistent with the observation that PDE-based method moves the interface. In opposition, the evolution of the sphericity for the geometric redistanciation is smooth, indicating that the method does not alter significantly the interfacial dynamics. Additionally, the geometric results are in better agreement with the reference data.

For the projection-based method, large oscillations dominate the sphericity evolution, and the results are not comparable to the reference curves. The behavior of the sphericity is assumed to be linked to the staircase shape reported in Figure 7, where the interface follows the underlying Cartesian mesh. For the lower frequency of $f = 1/(100\Delta t)$, the sphericity evolution is in the expected range, despite the presence of smaller oscillations.

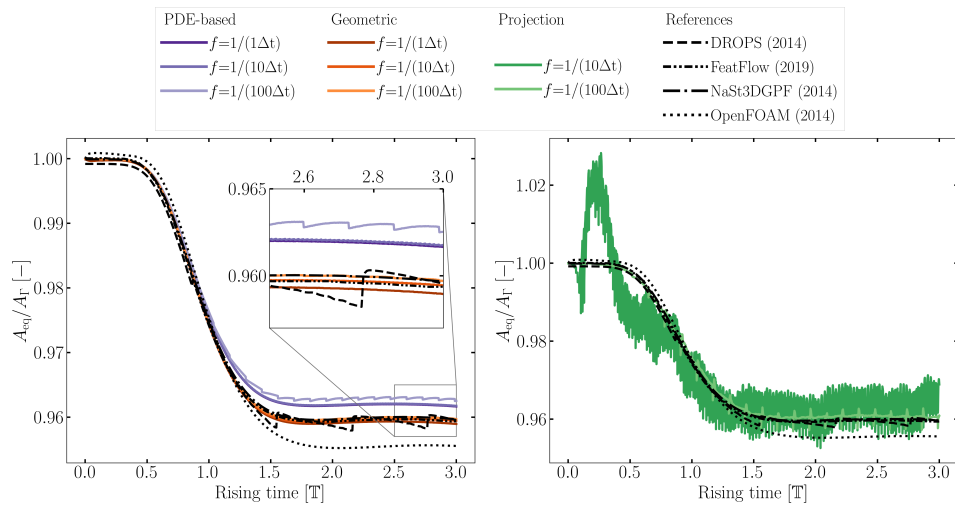


Figure 11: Comparison of the sphericity evolution for the different reinitialization methods at different reinitialization frequencies with reference values [19, 32]. On the left panel, the geometric reinitialization results capture an evolution similar to references (with the exception of OpenFOAM [32]) while, the PDE-based reinitialization results stabilize at an higher value. On the left panel, the projection-based reinitialization leads to nonphysical oscillations.

4.1.5. Selection of the Reinitialization Parameter Values

The comparison presented in this section and the following result from careful selection of the parameter values for each method. For the PDE-based

approach, they are challenging to select due to their number and coupled effects on the solution. For the value of interface thickness measure ε , Olsson et al. [6] suggest $\varepsilon \propto h$. Higher values ($\varepsilon > h$) lead to poor artificial time convergence to the steady-state or nonphysical oscillations of the phase indicator at the interface. The selected artificial time step $\Delta\tau$ has to enable convergence to steady-state efficiently. A too small value requires a significant number of time-steps (> 100) to reach steady-state, while a large value results in a nonphysical solution. Zahedi et al. [25] suggest $\Delta\tau = \min(\Delta t, h)$. In the present case, it leads to $\Delta\tau = \Delta t$. The value of the steady-state criterion has a similar effect. This work consider a value of 1×10^{-4} to ensure that the error remaining on the steady-state does not affect the results. For the maximum number of artificial time steps, this work considers a high value of 10000 to ensure convergence to the steady-state. Typically, the method reaches the steady-state criterion 1×10^{-4} within less than 10 artificial time steps.

For the geometric redistanciation, ε is proportional to the cell size at the interface. Values of ε higher than $2h$ leads to better volume conservation at lower reinitialization frequencies. For the maximum redistanciation distance, the current framework considers $d_{\max} \propto \varepsilon$. Typical values are $d_{\max} > 4\varepsilon$. A higher value d_{\max} results in additional computation time, but the parameter has no significant effect on the solution, as long as $d_{\max} > 4\varepsilon$.

Even if the PDE-based and geometric methods lead to the same tanh profile, as presented in Table 1, this work considers different values of ε to report the best results for both approaches. The reason why the same interface thickness does not lead to the same result quality is yet to be investigated.

For the projection-based reinitialization, the iso-level c is 0.5 to avoid any displacement of the interface, as explained in Section 3.3, and the sharpening parameter α is 1.5 as proposed by Aliabadi and Tezduyar [10].

4.2. Capillary Migration

This case considers a spherical droplet in 3D subjected to a ST coefficient gradient ($\nabla_{\Gamma}\gamma \neq 0$). In the absence of external force, a creeping flow develops due to the Marangoni effects described by Equation (18). The droplet keeps its spherical shape while migrating along the ST coefficient gradient towards the lowest ST region.

This application case considers a linear variation of the ST coefficient according to the x -position such that:

$$\gamma = \gamma_0 + \gamma' x \quad (41)$$

At steady-state, the droplet migrates along the x -axis at a velocity of [20]:

$$U = -\frac{2R}{3\mu_0(2+3\lambda)}\gamma' \quad (42)$$

where R is the radius of the droplet and $\lambda = \mu_1/\mu_0$ is the ratio of dynamic viscosities between the inside and outside of the droplet.

In opposition to the gravity-driven rising bubble case, the droplet migration results only from the tangential motion of the interface. Hence, capturing the analytical solution in a numerical framework requires an accurate representation of the interface throughout the time.

4.2.1. Description of the Case

Figure 12 presents the schematic of the case and Table 5 lists the selected properties, based on the work of Buscaglia and Ausas [20]. The bubble radius

is $R = 0.25\mathbb{L}$ and the domain is a cube with a side length of $12R$. For all boundaries, the case considers no-slip conditions for the velocity and no-flux conditions for the phase indicator. The initial condition imposes the droplet in the center of the domain, according to Equations (34) and (35), with both fluids at rest. The case considers a migration time of $3\mathbb{T}$.

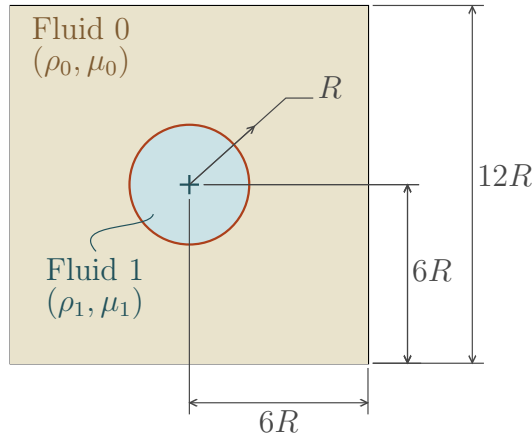


Figure 12: 2D cross-section view in the x - y plane of the initial state of the capillary migration case

Table 5: Physical properties of the capillary migration case

Parameters	Dimensions	Values
Density ratio (ρ_0/ρ_1)	-	1.0
Density of fluid 0 (ρ_0)	$\mathbb{M}\mathbb{L}^{-3}$	1.0
Viscosity ratio (μ_0/μ_1)	-	1.0
Dynamic viscosity of fluid 0 (μ_0)	$\mathbb{M}\mathbb{L}^{-1}\mathbb{T}^{-1}$	1.0
Reference ST coefficient (γ_0)	$\mathbb{M}\mathbb{T}^{-2}$	3.0
ST coefficient gradient (γ')	$\mathbb{M}\mathbb{T}^{-2}\mathbb{L}^{-1}$	-1.0

4.2.2. Metrics of Interest

The analysis focuses on two metrics of interest: the average velocity along the x -axis inside the droplet, corresponding to the migration velocity, and the radius distribution along the interface at the end of the simulation. The definition of the former is analogous to the definition of the rise velocity in the rising bubble case:

$$\text{Migration velocity} = \frac{\int_{\Omega} u_x \hat{H}_{\Gamma} d\Omega}{\int_{\Omega} \hat{H}_{\Gamma} d\Omega} \quad (43)$$

with Equation (42) corresponding to the analytical value. The radius distribution along the interface is:

$$r(\mathbf{x}) = \|\mathbf{x} - \mathbf{x}_b\| \quad \forall \mathbf{x} \in \Gamma \quad (44)$$

$$\mathbf{x}_b = \frac{\int_{\Omega} \mathbf{x} \hat{H}_{\Gamma} d\Omega}{\int_{\Omega} \hat{H}_{\Gamma} d\Omega} \quad (45)$$

where \mathbf{x}_b is the position of the droplet barycenter computed according to Equation (45). The analytical solution predicts a spherical droplet of constant radius R .

4.2.3. Simulation Settings

In the same fashion as the rising bubble case, this application assesses the effects of the three reinitialization methods and investigates three reinitialization frequencies: $f = 1/(N_{\text{reinit}} \Delta t)$, with $N_{\text{reinit}} \in \{1, 10, 100\}$.

An adaptively refined Cartesian grid discretizes the domain. The minimal and maximal cell sizes are $7.81 \times 10^{-3} \mathbb{L}$ and $6.25 \times 10^{-2} \mathbb{L}$, respectively. The time step is constant and set to $\Delta t = 1.3 \times 10^{-3} \mathbb{T}$. It is higher than the capillary limit described by Equation (40) to enable reasonable reinitialization CFL values. Experience and the results presented in this section show

that this choice does not lead to any stability issue. The CFL stabilizes at averaged values of 0.010, 0.011, and 0.007 for the PDE-based, geometric, and projection-based methods, respectively.

The geometric and projection-based methods use the same specific parameters as in the rising bubble case. For the PDE-based approach, the value of the interface thickness measure ε changes, yielding to better results than if the same value as in the rising bubble case is used. It highlights that the parameter selection for the PDE-based approach is case dependent.

4.2.4. Results

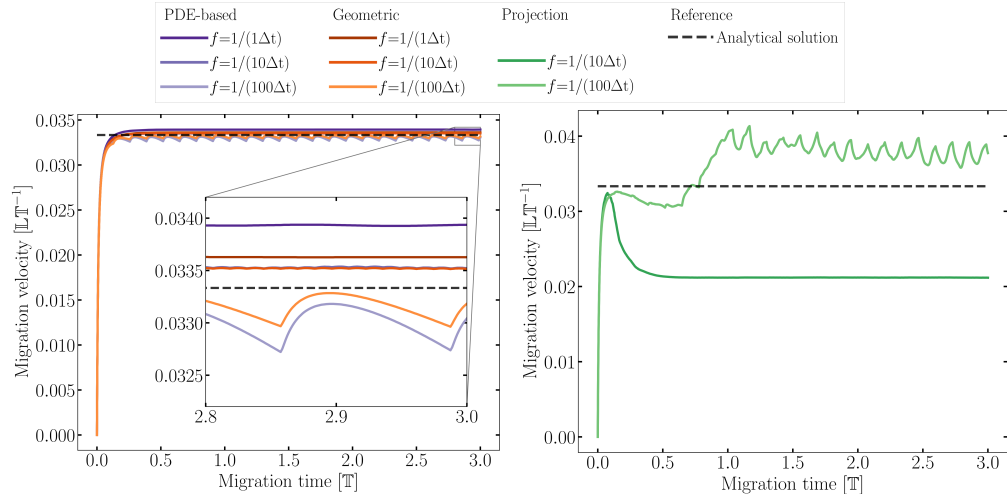
Figure 13 presents the evolution of the migration velocity and Figure 14 displays the radius distribution in the xy -plane with respect to the azimuthal angle at the end of the simulation time. Overlays of the iso-surface $\phi = 0.5$ give an insight of the overall shape of the droplet at the end of the simulation.

The PDE-based reinitialization and the geometric redistanciation result in migration velocities in good agreement with the analytical value for all frequencies. Both methods leads to velocity variations due to the reinitialization frequency at $f = 1/(100\Delta t)$. It highlights the importance of the reinitialization in this case: as the phase indicator diffuses between two reinitialization steps, the bubble slows down. When applied, the reinitialization method recovers a sharper indicator field and the bubble tends toward the expected migration velocity.

The final radius distribution for the PDE-based method, presented in the left plot of Figure 14, oscillates smoothly around a value close to the expected sphere radius for all frequencies. The geometric method (Figure 14, right plot) results in the same behavior for $f \in \{1/(10\Delta t), 1/(100\Delta t)\}$,

while the reinitialization frequency of $1/\Delta t$ leads to stronger and sharper oscillations. Additionally, these variations are asymmetric with respect to the front and tail of the droplet. For this frequency ($1/\Delta t$), the reinitialization CFL is approximately 0.01 for the PDE-based and geometric methods, which corresponds to almost one order of magnitude lower than in the rising bubble case. It leads to a negative impact on the droplet shape for the geometric method, while it has no effect on the PDE-based results, as highlighted in Figure 14. In this specific test case, the geometric method does not perform as well at low reinitialization CFL.

Figure 14 reveals that the projection-based reinitialization leads to strong oscillations of the radius and it fails to capture the migration of the droplet for all frequencies, as presented in Figure 13.



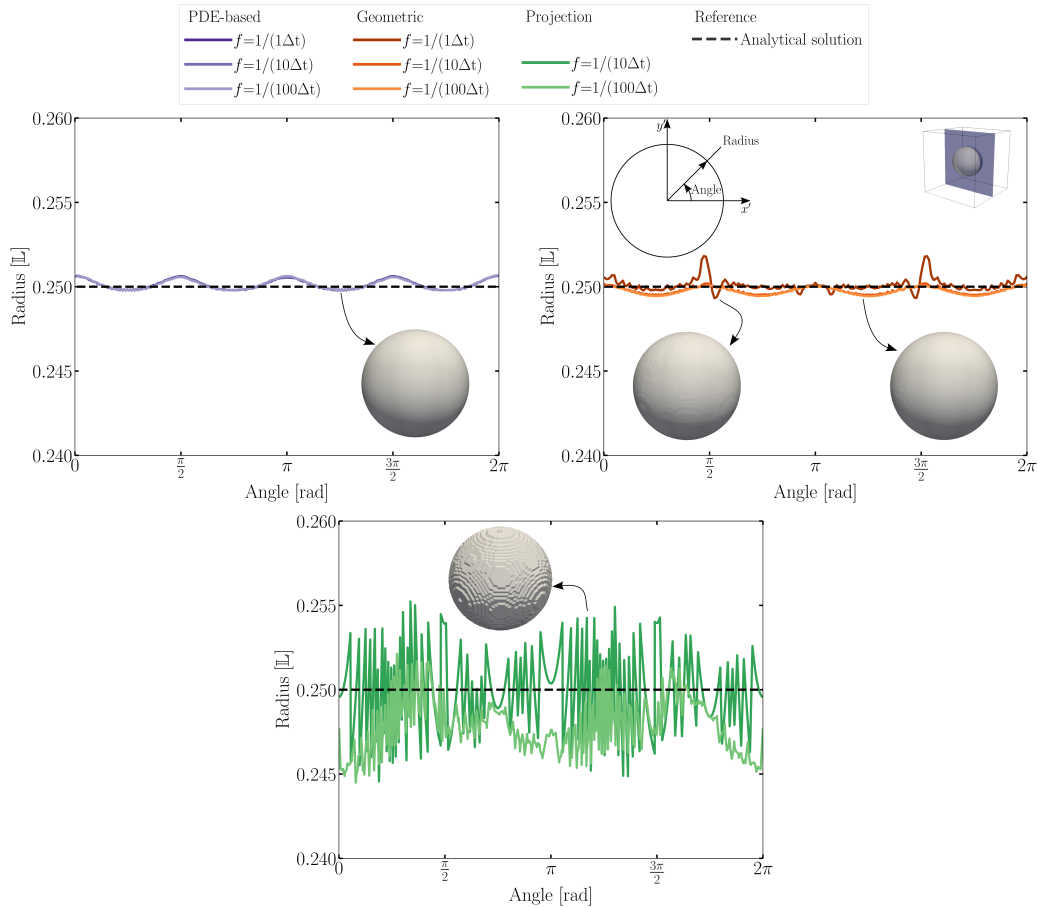


Figure 14: Comparison of the final radius distribution in the x - y plane with respect to the azimuthal angle for the different reinitialization methods at different reinitialization frequencies. On the left panel, the PDE-based reinitialization results indicate a smooth quasi-spherical droplet. On the right panel, the geometric reinitialization results capture expected shape for the lower frequencies. However, at the highest frequency, oscillations appear at the surface of the droplet. Lastly on the bottom panel, the projection-based results display a poor conservation of the spherical shape.

4.3. Rayleigh-Plateau Instability

The Rayleigh-Plateau instability is a case where the ST force has a destabilizing effect, in opposition to the two previous applications. For a capillary liquid jet, the instability acts to reduce the surface energy of the jet, leading to its breakup into droplets [21]. It is a 3D case with complex interfacial deformations and the current work uses it to assess the spatial convergence of the reinitialization methods. Due to the poor performances of the projection-based method in the previous cases and this one, this study focuses only on the PDE-based and geometric approaches.

4.3.1. Case Description

Figure 15 shows the schematic of the case. The domain is a rectangular prism of dimensions $80R \times 20R \times 20R$, where R is the radius of the jet at the inlet. The jet axis corresponds to the x -axis of the domain.

Based on the work of Denner et al. [21], the jet undergoes a periodic perturbation through the x -component of inlet velocity U_{inlet}^* , imposed at the left side of the domain, according to:

$$U_{\text{inlet}}^* = \begin{cases} 0 & \forall \mathbf{x} \in \Omega_0 \\ U_{\text{inlet}} \left(1 + \delta_0 \sin \left(\frac{k_{\text{jet}} U_{\text{inlet}} t}{R} \right) \right) & \forall \mathbf{x} \in \Omega_1 \end{cases} \quad (46)$$

where U_{inlet} is the unperturbed inlet velocity, δ_0 is the dimensionless excitation amplitude, and k_{jet} is the dimensionless wavenumber. The case considers $R = 1.145 \times 10^{-3}$ m, $\delta_0 = 0.3$, $k_{\text{jet}} = 0.7$, and the physical properties listed in Table 6. It corresponds to an Ohnesorge number ($\text{Oh} = \mu_1 / \sqrt{\gamma \rho_1 R}$) of 0.1. The selected Weber number ($\text{We} = \rho_1 R U_{\text{inlet}}^2 / \gamma$) is 50, which results in $U_{\text{inlet}} = 1.569$ m s⁻¹.

For the NS equations, the case imposes the Dirichlet boundary condition $\mathbf{u} = [U_{\text{inlet}}^*, 0, 0]^T$ at the left boundary, and outlet conditions at the other boundaries. For the phase indicator, it imposes a Dirichlet condition at the left boundary according to:

$$\phi_{\text{jet}}(\mathbf{x}) = 0.5 - 0.5 \tanh\left(\frac{d_{\text{jet}}(\mathbf{x})}{2\varepsilon}\right) \quad (47)$$

$$d_{\text{jet}}(\mathbf{x}) = \sqrt{y^2 + z^2} - R \quad (48)$$

where d_{jet} is the signed distance from the unperturbed jet interface. It considers no-flux conditions at the remaining boundaries.

The initial condition imposes a uniform velocity of $\mathbf{u}_0 = [U_{\text{inlet}}, 0, 0]^T$ in the jet, and null elsewhere. For the phase indicator, it follows Equations (47) and (48). The simulation time is 0.08 s.

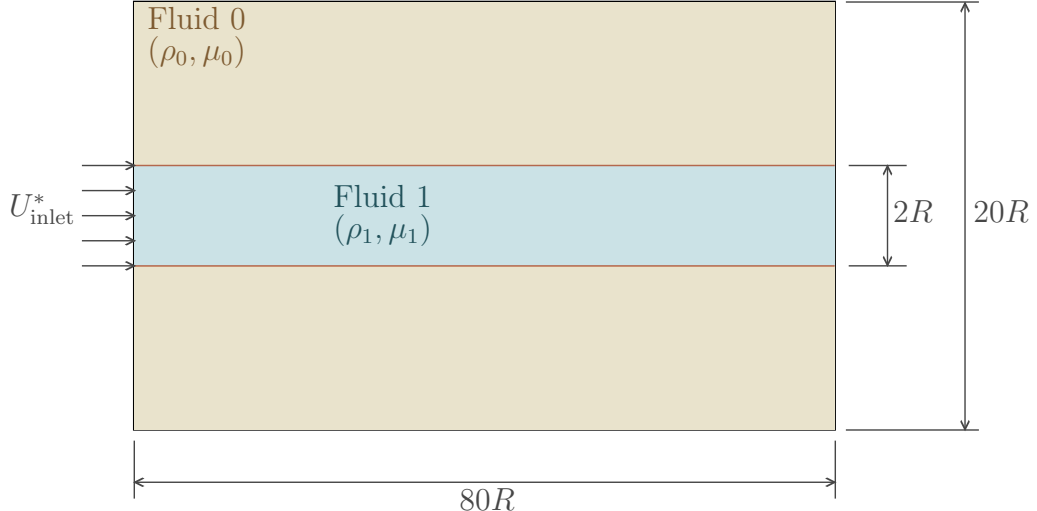


Figure 15: 2D cross-section view in the x - y plane of the initial state of the Rayleigh-Plateau case, where Fluid 1 corresponds to the liquid jet

Table 6: Physical properties of the Rayleigh-Plateau instability case

Parameters	Units	Values
Density ratio (ρ_0/ρ_1)	-	1×10^{-3}
Density of fluid 0 (ρ_0)	kg m^{-3}	1.196
Viscosity ratio (μ_0/μ_1)	-	1×10^{-2}
Dynamic viscosity of fluid 0 (μ_0)	$\text{kg m}^{-1} \text{s}^{-1}$	3.038×10^{-4}
ST coefficient (γ)	kg s^{-2}	6.740×10^{-2}

4.3.2. Metric of Interest

The surface energy E_Γ of the jet drives the development of the instability [1]:

$$E_\Gamma = \gamma A_\Gamma \quad (49)$$

where A_Γ is the surface area of the jet. Hence, the metric of interest is the relative surface area of the jet $A_\Gamma/A_{\Gamma,0}$, with $A_{\Gamma,0}$ corresponding to the surface area of the jet at $t = 0$ s. The surface area computation follows the method described in Section 4.1.2. This case also monitors the relative volume evolution, computed according to Equation (38).

4.3.3. Simulation Settings

To assess the spatial convergence, this study monitors $A_\Gamma/A_{\Gamma,0}$ and V/V_0 for four adaptively refined Cartesian meshes, reported in Table 7. It considers a constant CFL of 0.25 for all meshes, which also ensures the respect of the capillary time step limit (Equation (40)).

The study restricts itself to only one reinitialization frequency of $f = 1/(10\Delta t)$. This choice aims to limit the growth of parasitic capillary waves, described

by Denner et al. [39], without introducing additional artificial diffusion or limiters. Additionally, as denoted at the bottom of Table 2, this study deactivates the approximation \hat{H}_Γ described by Equation (17) for the PDE-based method to report better volume conservation and spacial convergence. It considers instead $\hat{H}_\Gamma(\mathbf{x}) = \phi(\mathbf{x})$.

Table 7: Refinement levels for the Rayleigh-Plateau instability convergence study. $R = 1.145 \times 10^{-3}$ m. The approximate number of cells is reported for the initial jet and changes for the PDE-based and geometric methods due to difference values of ε (h and $3h$, respectively).

Ref. level	Approx. no. cells (PDE)	Approx. no. cells (Geo.)	Max. cell size	Min. cell size
Coarse	3.6×10^5	7.1×10^5	$1.25R$	$0.16R$
Medium	1.5×10^6	2.5×10^6	$0.63R$	$0.08R$
Fine	6.4×10^6	1.1×10^7	$0.31R$	$0.04R$
Extra-fine	3.0×10^7	4.6×10^7	$0.16R$	$0.02R$

4.3.4. Results

Figures 16 and 17 present the spatial convergence of the relative volume and surface, respectively. For both methods, the results reveal two regimes with a transition around 0.05 s. The first one presents small oscillations, corresponding to the imposed perturbations of the jet flow rate at the inlet. The second regimes features stronger and sharper oscillations, which corresponds to droplets exiting the computational domain.

For the geometric method, the relative volume converges in space to a periodic oscillation around $V/V_0 \approx 1$ in the first regime, which is the expected result if the solver conserves the volume. Its mesh convergence in

the second regime is slower, indicating a slower convergence of the shape of the droplets generated by the breakup. Indeed, the relative surface evolution converges for the fine and extra-fine meshes until approximately 0.02 s. This time corresponds to the beginning of the necking of the jet leading to the first breakup. The slower mesh convergence following the breakup indicates that the jet and droplet shapes change with the spatial discretization when the Rayleigh-Plateau instability grows stronger, even if the volume does not change significantly. The results for the coarse mesh is significantly different due to propagation of parasitic capillary waves, and the plot leaves out part of the evolution for the sake of clarity.

The relative volume obtained with PDE-based reinitialization tends to converge towards a similar solution as the geometric approach, but at a slower rate in the second regime. Additionally, it leads to a volume increase in the first regime, which is not observed with the geometric method. For the surface evolution, the difference between the fine and extra fine meshes grows with time, also indicating that the method reaches convergence at a slower rate for the jet and droplet shapes than the relative volume.

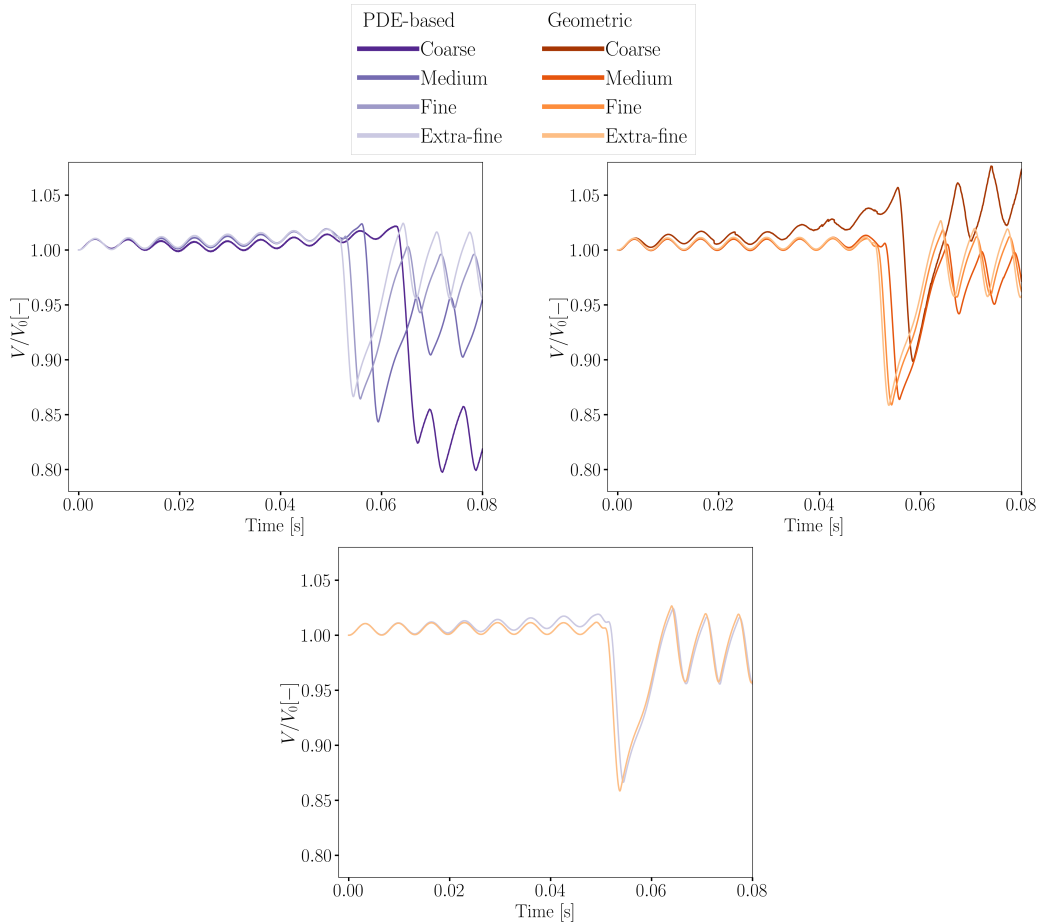


Figure 16: Spatial convergence of the relative volume for the Rayleigh-Plateau case. On the top-left panel, the PDE-based reinitialization leads to the convergence of the relative volume to a value oscillating slightly above 1 for $t < 0.05$ s. Then, for $t > 0.05$ s, the convergence is slower. On the top-right panel, the geometric method results in similar trends, with a relative volume oscillating around 1 for $t < 0.05$ s and a faster convergence rate than the PDE-based approach for $t > 0.05$ s. The bottom panel presents the comparison of the two methods results for the extra-fine meshes, highlighting that both methods converge toward similar solutions.

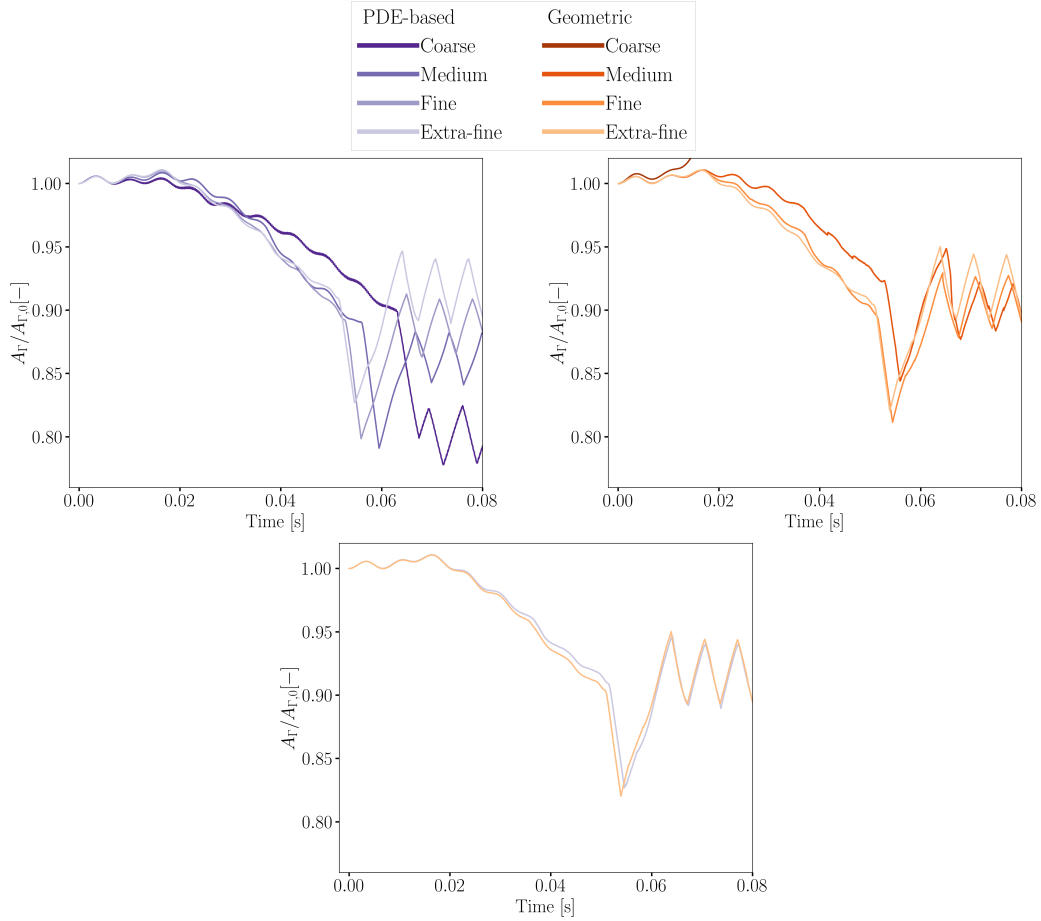


Figure 17: Spatial convergence of the relative surface for the Rayleigh-Plateau case. On the top-left panel, the PDE-based reinitialization leads to the convergence of the relative surface, with a slower rate for $t > 0.05$ s. On the top-right panel, the geometric method results in similar trends, however the difference between the two finest meshes is smaller for $t > 0.05$ s than the PDE-based approach. The bottom panel presents the comparison of the two methods for the extra-fine meshes: they result in relative surface evolutions in great agreement.

5. Conclusion

This work focuses on capillary flows and on the need of reinitialization methods to capture with accuracy and robustness the interfacial dynamics. It presents the complete problem formulation in an open-source level-set-based FEM framework along with three reinitialization approaches: a PDE-based method, a novel geometric approach, and a simple projection-based method.

The work provides an objective comparative study of the three reinitialization methods using three application cases: the 3D rising bubble benchmark, the capillary migration, and the Rayleigh-Plateau instability. The study focuses on sensitive metrics such as the volume enclosed by the interface, its surface area (or sphericity) and radius distribution. This choice of metrics is important to ensure thorough assessment of the method's accuracy and robustness. The study also includes a sweep on the reinitialization frequency for the rising bubble and capillary migration cases, and a spatial converge analysis on the Rayleigh-Plateau instability case.

The results show good agreement with reference data and low sensitivity to the frequency for the PDE-based and geometric approaches in the rising bubble and capillary migration. Yet, the PDE-based reinitialization leads to artificial displacement of the interface, while the geometric approach maintains the interface position, but is more sensitive to a low reinitialization CFL. For the Rayleigh-Plateau instability case, the PDE-based and geometric methods converge in space, however the latter leads to a better accuracy of the volume and surface for coarser meshes.

The projection-based method does not capture the interfacial dynamics for the rising bubble and capillary migration and demonstrates poor perfor-

mance. Therefore, the comparison omits the projection-based method for the Rayleigh-Plateau instability case.

This work highlights that the state-of-the-art PDE-based method results quality depends on the selection of four parameters, which are case-dependent, while the results of the geometric method does not change throughout the cases for a same set of two parameters, which makes it more robust.

Finally, future works include application of the geometric method to complex multi-physics flows such as in the laser powder bed fusion process, in which significant interfacial deformations are driven by large evaporation- and capillary-induced pressure jumps as well as Marangoni effects. This type of case would benefit from the robustness offered by the two-parameter geometric framework.

6. Acknowledgment

The authors acknowledge the technical support and computing time provided by the Digital Research Alliance of Canada. HPL and AA acknowledge financial support from the Natural Sciences and Engineering Research Council of Canada (NSERC) and the Fonds de recherche du Québec – Nature et technologies (FRQNT). MSF acknowledges financial support by the European Research Council through the ERC Starting Grant ExcelAM under award number 101117579. BB acknowledges financial support from the Natural Sciences and Engineering Research Council of Canada (NSERC) through the RGPIN-2020-04510 Discovery Grant and the funding from the Multiphysics Multiphase Intensification Automatization Workbench (MMIAOW) Canadian Research Chair Level 2 in computer-assisted design and scale-up

of alternative energy vectors for sustainable chemical processes (CRC-2022-00340).

References

- [1] P.-G. Gennes, F. Brochard-Wyart, D. Quéré, *Gouttes, bulles, perles et ondes*, deuxieme ed., Belin, Paris, FR, 2005.
- [2] S. Popinet, Numerical models of surface tension, *Annual Review of Fluid Mechanics* 50 (2018) 49–75. URL: <https://www.annualreviews.org/content/journals/10.1146/annurev-fluid-122316-045034>. doi:<https://doi.org/10.1146/annurev-fluid-122316-045034>.
- [3] P. S. Cook, A. B. Murphy, Simulation of melt pool behaviour during additive manufacturing: Underlying physics and progress, *Additive Manufacturing* 31 (2020) 100909. URL: <https://www.sciencedirect.com/science/article/pii/S2214860419305731>. doi:<https://doi.org/10.1016/j.addma.2019.100909>.
- [4] D. Fuster, Y. Mimoh, Regularization errors introduced by the one-fluid formulation in the solution of two-phase elliptic problems, *Journal of Computational Physics* 514 (2024) 113202. URL: <https://www.sciencedirect.com/science/article/pii/S0021999124004510>. doi:<https://doi.org/10.1016/j.jcp.2024.113202>.
- [5] G. Tryggvason, R. Scardoveli, S. Zaleski, *Direct Numerical Simulations of Gas-Liquid Multiphase Flows*, first ed., Cambridge University Press, Cambridge, UK, 2011.
- [6] E. Olsson, G. Kreiss, S. Zahedi, A conservative level set method for two phase flow ii, *Journal of Computational Physics* 225 (2007) 785–807. URL: <https://www.sciencedirect.com/science/article/pii/>

S0021999107000046. doi:<https://doi.org/10.1016/j.jcp.2006.12.027>.

- [7] S. Mirjalili, S. Jain, M. Dodd, Interface-capturing methods for two-phase flows: An overview and recent developments, Center for Turbulence Research - Annual research brief (2017) 117–135.
- [8] M. Garcia-Villalba, T. Colonius, O. Desjardins, D. Lucas, A. Mani, D. Marchisio, O. K. Matar, F. Picano, S. Zaleski, Numerical methods for multiphase flows, International Journal of Multiphase Flow 191 (2025) 105285. URL: <https://www.sciencedirect.com/science/article/pii/S0301932225001636>. doi:<https://doi.org/10.1016/j.ijmultiphaseflow.2025.105285>.
- [9] C. Hirt, B. Nichols, Volume of fluid (vof) method for the dynamics of free boundaries, Journal of Computational Physics 39 (1981) 201–225. URL: <https://www.sciencedirect.com/science/article/pii/0021999181901455>. doi:[https://doi.org/10.1016/0021-9991\(81\)90145-5](https://doi.org/10.1016/0021-9991(81)90145-5).
- [10] S. Aliabadi, T. E. Tezduyar, Stabilized-finite-element/interface-capturing technique for parallel computation of unsteady flows with interfaces, Computer Methods in Applied Mechanics and Engineering 190 (2000) 243–261. URL: <https://www.sciencedirect.com/science/article/pii/S0045782500002000>. doi:[https://doi.org/10.1016/S0045-7825\(00\)00200-0](https://doi.org/10.1016/S0045-7825(00)00200-0).
- [11] D. Fuster, Y. Mimoh, Regularization errors introduced by the one-fluid

approach in the solution of elliptic equations for multiphase flow problems, 2025. International Conference on Multiphase Flow.

- [12] R. F. Ausas, F. S. Sousa, G. C. Buscaglia, An improved finite element space for discontinuous pressures, *Computer Methods in Applied Mechanics and Engineering* 199 (2010) 1019–1031. URL: <https://www.sciencedirect.com/science/article/pii/S0045782509003867>. doi:<https://doi.org/10.1016/j.cma.2009.11.011>.
- [13] R. F. Ausas, E. A. Dari, G. C. Buscaglia, A geometric mass-preserving redistancing scheme for the level set function, *International Journal for Numerical Methods in Fluids* 65 (2011) 989–1010. URL: <https://onlinelibrary.wiley.com/doi/abs/10.1002/fld.2227>. doi:<https://doi.org/10.1002/fld.2227>. arXiv:<https://onlinelibrary.wiley.com/doi/pdf/10.1002/fld.2227>.
- [14] F. Henri, M. Coquerelle, P. Lubin, Geometrical level set reinitialization using closest point method and kink detection for thin filaments, topology changes and two-phase flows, *Journal of Computational Physics* 448 (2022) 110704. URL: <https://www.sciencedirect.com/science/article/pii/S0021999121005994>. doi:<https://doi.org/10.1016/j.jcp.2021.110704>.
- [15] O. Desjardins, V. Moureau, H. Pitsch, An accurate conservative level set/ghost fluid method for simulating turbulent atomization, *Journal of Computational Physics* 227 (2008) 8395–8416. URL: <https://www.sciencedirect.com/science/article/pii/S0021999108003112>. doi:<https://doi.org/10.1016/j.jcp.2008.05.027>.

- [16] R. Chiodi, O. Desjardins, A reformulation of the conservative level set reinitialization equation for accurate and robust simulation of complex multiphase flows, *Journal of Computational Physics* 343 (2017) 186–200. URL: <https://www.sciencedirect.com/science/article/pii/S0021999117303327>. doi:<https://doi.org/10.1016/j.jcp.2017.04.053>.
- [17] M. Sussman, P. Smereka, S. Osher, A level set approach for computing solutions to incompressible two-phase flow, *Journal of Computational Physics* 114 (1994) 146–159. URL: <https://www.sciencedirect.com/science/article/pii/S0021999184711557>. doi:<https://doi.org/10.1006/jcph.1994.1155>.
- [18] S. Hysing, S. Turek, D. Kuzmin, N. Parolini, E. Burman, S. Ganesan, L. Tobiska, Quantitative benchmark computations of two-dimensional bubble dynamics, *International Journal for Numerical Methods in Fluids* 60 (2009) 1259–1288. URL: <https://onlinelibrary.wiley.com/doi/abs/10.1002/fld.1934>. doi:<https://doi.org/10.1002/fld.1934>. arXiv:<https://onlinelibrary.wiley.com/doi/pdf/10.1002/fld.1934>.
- [19] S. Turek, O. Mierka, K. Bäumler, Numerical benchmarking for 3d multiphase flow: New results for a rising bubble, in: F. A. Radu, K. Kumar, I. Berre, J. M. Nordbotten, I. S. Pop (Eds.), *Numerical Mathematics and Advanced Applications ENUMATH 2017*, Springer International Publishing, Cham, 2019, pp. 593–601.
- [20] G. C. Buscaglia, R. F. Ausas, Variational formulations for surface tension, capillarity and wetting, *Computer Methods in Applied*

Mechanics and Engineering 200 (2011) 3011–3025. URL: <https://www.sciencedirect.com/science/article/pii/S0045782511002209>. doi:<https://doi.org/10.1016/j.cma.2011.06.002>.

- [21] F. Denner, F. Evrard, A. A. Castrejón-Pita, J. R. Castrejón-Pita, B. van Wachem, Reversal and inversion of capillary jet breakup at large excitation amplitudes, Flow Turbulence Combust 108 (2022) 843–863. URL: <https://link.springer.com/article/10.1007/s10494-021-00291-w>. doi:<https://doi.org/10.1007/s10494-021-00291-w>.
- [22] A. Alphonius, L. Barbeau, B. Blais, O. Gaboriault, O. Guévremont, J. Lamouche, P. Laurentin, O. Marquis, P. Munch, V. Ferreira, H. Papillon-Laroche, P. Patience, L. Prieto Saavedra, M. Vaillant, Lethe 1.0: An open-source high-performance and high-order computational fluid dynamics software for single and multiphase flows, 2025. doi:[10.2139/ssrn.5090483](https://doi.org/10.2139/ssrn.5090483).
- [23] T. E. Tezduyar, Stabilized finite element formulations for incompressible flow computations, in: Adv. Appl. Math., volume 28, Elsevier, 1991, pp. 1–44. URL: [https://doi.org/10.1016/S0065-2156\(08\)70153-4](https://doi.org/10.1016/S0065-2156(08)70153-4).
- [24] J. Brackbill, D. Kothe, C. Zemach, A continuum method for modeling surface tension, Journal of Computational Physics 100 (1992) 335–354. URL: <https://www.sciencedirect.com/science/article/pii/002199919290240Y>. doi:[https://doi.org/10.1016/0021-9991\(92\)90240-Y](https://doi.org/10.1016/0021-9991(92)90240-Y).

[25] S. Zahedi, M. Kronbichler, G. Kreiss, Spurious currents in finite element based level set methods for two-phase flow, *International Journal for Numerical Methods in Fluids* 69 (2012) 1433–1456. URL: <https://onlinelibrary.wiley.com/doi/abs/10.1002/fld.2643>. doi:<https://doi.org/10.1002/fld.2643>.

[26] D. Arndt, W. Bangerth, M. Bergbauer, B. Blais, M. Fehling, R. Gassmöller, T. Heister, L. Heltai, M. Kronbichler, M. Maier, P. Munch, S. Scheuerman, B. Turcksin, S. Uzunbajakau, D. Wells, M. Wichrowski, The deal.ii library, version 9.7, *Journal of Numerical Mathematics* 33 (2025) 403–415. doi:10.1515/jnma-2025-0115.

[27] C. Burstedde, L. C. Wilcox, O. Ghattas, p4est: Scalable algorithms for parallel adaptive mesh refinement on forests of octrees, *SIAM J. Sci. Comput.* 33 (2011) 1103–1133. URL: <https://doi.org/10.1137/100791634>.

[28] D. W. Kelly, J. P. De S. R. Gago, O. C. Zienkiewicz, I. Babuska, A posteriori error analysis and adaptive processes in the finite element method: Part i—error analysis, *International Journal for Numerical Methods in Engineering* 19 (1983) 1593–1619. URL: <https://onlinelibrary.wiley.com/doi/abs/10.1002/nme.1620191103>. arXiv:<https://onlinelibrary.wiley.com/doi/pdf/10.1002/nme.1620191103>.

[29] P.-H. Chiu, Y.-T. Lin, A conservative phase field method for solving incompressible two-phase flows, *Journal of Computational Physics* 230 (2011) 185–204. URL: <https://www.sciencedirect.com/science>

article/pii/S0021999110005243. doi:<https://doi.org/10.1016/j.jcp.2010.09.021>.

- [30] F. Mut, G. C. Buscaglia, E. A. Dari, New mass-conserving algorithm for level set redistancing on unstructured meshes, *Journal of Applied Mechanics* 73 (2006) 1011–1016. URL: <https://doi.org/10.1115/1.2198244>. doi:10.1115/1.2198244. arXiv:https://asmedigitalcollection.asme.org/appliedmechanics/article-pdf/73/6/1011/5475370/1011_1.pdf.
- [31] W. Bangerth, O. Kayser-Herold, Data structures and requirements for hp finite element software, *ACM Trans. Math. Softw.* 36 (2009) 4/1–4/31.
- [32] J. Adelsberger, P. Esser, M. Griebel, S. Groß, M. Klitz, A. Rüttgers, 3D incompressible two-phase flow benchmark computations for rising droplets, Report, Institut für Numerische Simulation (INS), 2014. URL: <https://bonndoc.ulb.uni-bonn.de/xmlui/handle/20500.11811/11908>.
- [33] S. Gross, A. Reusken, Numerical Methods for Two-phase Incompressible Flows, volume 40 of *Springer Series in Computational Mathematics*, Springer, Berlin, Heidelberg, 2011. URL: <https://link.springer.com/10.1007/978-3-642-19686-7>. doi:10.1007/978-3-642-19686-7.
- [34] IGPM, Drops | IGPM, 2025. URL: <https://www.igpm.rwth-aachen.de/forschung/drops>, accessed: 2025-09-03.

[35] S. Turek, C. Becker, FeatFlow User Manual Release 1.1, 1998. URL: <https://wwwold.mathematik.tu-dortmund.de/~featflow/media/download/featflow.pdf>.

[36] R. Croce, M. Griebel, M. A. Schweitzer, Numerical simulation of bubble and droplet deformation by a level set approach with surface tension in three dimensions, *International Journal for Numerical Methods in Fluids* 62 (2010) 963–993. URL: <https://onlinelibrary.wiley.com/doi/abs/10.1002/fld.2051>. doi:10.1002/fld.2051.

[37] M. Engel, NaSt3DGPF - A Parallel 3D Flow Solver, 2009. URL: <https://ins.uni-bonn.de/media/public/u/griebel/NaSt3DGPF/>, accessed: 2025-09-03.

[38] H. Scheufler, J. Roenby, TwoPhaseFlow: A Framework for Developing Two Phase Flow Solvers in OpenFOAM, *OpenFOAM® Journal* 3 (2023) 200–224. URL: <https://journal.openfoam.com/index.php/ofj/article/view/80>. doi:10.51560/ofj.v3.80.

[39] F. Denner, F. Evrard, R. Serfaty, B. G. van Wachem, Artificial viscosity model to mitigate numerical artefacts at fluid interfaces with surface tension, *Computers & Fluids* 143 (2017) 59–72. URL: <https://www.sciencedirect.com/science/article/pii/S0045793016303565>. doi:<https://doi.org/10.1016/j.compfluid.2016.11.006>.